Available online at www.sciencedirect.com

SCIENCE DIRECT®

Journal of Computational Physics 207 (2005) 309–353

JOURNAL OF COMPUTATIONAL PHYSICS

www.elsevier.com/locate/jcp

Simultaneous solution algorithms for Eulerian–Eulerian gas–solid flow models: Stability analysis and convergence behaviour of a point and a plane solver

Juray De Wilde [a,b,*], Jan Vierendeels [b], Geraldine J. Heynderickx [a], Guy B. Marin [a]

[a] *Laboratorium voor Petrochemische Techniek, Ghent University, Krijgslaan 281, Blok S5, B-9000 Ghent, Belgium*
[b] *Fluid Mechanics Laboratory, Department of Fluid, Heat and Combustion Mechanics, Ghent University, St.-Pietersnieuwstraat 41, B-9000 Ghent, Belgium*

Received 13 April 2004; received in revised form 29 October 2004; accepted 18 January 2005
Available online 17 March 2005

Abstract

Simultaneous solution algorithms for Eulerian–Eulerian gas–solid flow models are presented and their stability analyzed.

The integration algorithms are based on dual-time stepping with fourth-order Runge–Kutta in pseudo-time. The domain is solved point or plane wise. The discretization of the inviscid terms is based on a low-Mach limit of the multi-phase preconditioned advection upstream splitting method (MP-AUSMP).

The numerical stability of the simultaneous solution algorithms is analyzed in 2D with the Fourier method. Stability results are compared with the convergence behaviour of 3D riser simulations.

The impact of the grid aspect ratio, preconditioning, artificial dissipation, and the treatment of the source terms is investigated. A particular advantage of the simultaneous solution algorithms is that they allow a fully implicit treatment of the source terms which are of crucial importance for the Eulerian–Eulerian gas–solid flow models and their solution.

The numerical stability of the optimal simultaneous solution algorithm is analyzed for different solids volume fractions and gas–solid slip velocities. Furthermore, the effect of the grid resolution on the convergence behaviour and the simulation results is investigated.

Finally, simulations of the bottom zone of a pilot-scale riser with a side solids inlet are experimentally validated.

Keywords: Gas–solid flow; Eulerian–Eulerian approach; Numerical algorithm; Simultaneous solution algorithm; Stability analysis; Point solver; Plane solver; Preconditioning; Advection upstream splitting method; Riser

---

[*] Corresponding author. Tel.: +32 9 264 45 16/32 97; fax: +32 9 264 49 99/35 86.
E-mail address: Guy.Marin@UGent.be (G.B. Marin).

0021-9991/$ - see front matter
doi:10.1016/j.jcp.2005.01.019

Nomenclature

Notations

c_g	gas phase speed of sound $[\mathrm{m\,s^{-1}}]$
c_m	mixture speed of sound, i.e., the propagation speed of gas phase pressure waves in the gas–solid mixture $[\mathrm{m\,s^{-1}}]$
$\tilde{c}$	numerical speed of sound $[\mathrm{m\,s^{-1}}]$
C_P	heat capacity at constant pressure $[\mathrm{J\,kg^{-1}\,K^{-1}}]$
d_p	particle diameter [m]
ds	spatial dimension [m]
D	drag source terms matrix
e_g	gas phase internal energy $[\mathrm{J\,kg^{-1}}]$
E_g	gas phase total energy $[\mathrm{J\,kg^{-1}}]$
e	restitution coefficient for particle–particle collisions [/]
e_wall	restitution coefficient for particle–wall collisions [/]
F	flux
$\bar{g}$	gravity $[\mathrm{m_r\,s^{-2}}]$
G	gravity source terms matrix
G_s	solids mass flux $[\mathrm{kg\,m^{-2}\,s^{-1}}]$
k	turbulent energy gas phase $[\mathrm{J\,kg^{-1}}]$
P	gas phase pressure $[\mathrm{N\,m^{-2}}]$
P_s	solid phase pressure $[\mathrm{N\,m^{-2}}]$
$q_{\mathrm{g}/s}$	kinetic energy gas/solid phase $[\mathrm{m^2\,s^{-2}}]$
Q	vector of the conservative variables
$\bar{r}$	position vector
s	speed $[\mathrm{m\,s^{-1}}]$
$\bar{\bar{s}}$	viscous stress tensor $[\mathrm{kg\,m^{-1}\,s^{-2}}]$
t	time [s]
T	temperature [K]
$\bar{u}$	local mean velocity gas phase $[\mathrm{m_r\,s^{-1}}]$
$\bar{v}$	local mean velocity solid phase $[\mathrm{m_r\,s^{-1}}]$
W	vector of the viscous variables

Greek notations

β	drag coefficient $[\mathrm{kg\,m^{-3}\,s^{-1}}]$
Γ	preconditioning matrix
γ	dissipation of kinetic fluctuation energy by inelastic particle–particle collisions $[\mathrm{kg\,m}_r^{-1}\,\mathrm{s^{-3}}]$
δ_ad	artificial dissipation parameter
ε	dissipation of turbulent kinetic energy of the gas phase $[\mathrm{m}_r^2\,\mathrm{s^{-3}}]$
ε_g	gas phase volume fraction $[\mathrm{m_g^3\,m_{reactor}^{-3}}]$
ϵ_s	solids volume fraction $[\mathrm{m_s^3\,m_{reactor}^{-3}}]$
Θ	granular temperature solid phase $[\mathrm{J\,kg^{-1}}]$
κ	conductivity kinetic fluctuation energy solid phase $[\mathrm{kg\,m^{-1}\,s^{-1}}]$
λ	eigenvalue
λ	conductivity $[\mathrm{W\,m^{-1}\,K^{-1}}]$
μ_g	molecular viscosity gas phase [Pa s]

μ_g^t	turbulent viscosity gas phase [Pa s]
μ_s	shear viscosity solid phase [kg m^{-1} s^{-1}]
ω	wave number
ξ_s	bulk viscosity solid phase [kg m^{-1} s^{-2}]
ρ_g	gas phase density [kg m^{-3}]
ρ_m	mixture density [kg m^{-3}]
ρ_{sp}	solid phase density [kg m^{-3}]
τ	pseudo-time [s]
ϕ	scalar quantity
ϕ	specularity factor for particle–wall collisions [/]
$\phi(\tau)$	pre-exponential factor
Ψ	error

Subscript

a	acoustic
c	convective
d	artificial dissipation
g	gas phase
i	of node i
i'	of neighbouring node i'
i''	of non-neighbouring node i''
ii'	at the cell interface between nodes i and i'
l	plane
s	solid phase
sp	solid phase
v	viscous
x	x direction
y	y direction
z	z direction

Superscript

_	vector
=	tensor
∧	perturbation
(a)	acoustic
(c)	convective
g	gas phase
n	pseudo-time step number
s	solid phase
T	transposed
(v)	viscous

Other

⟨⟩	mean
$\Im$	Fourier symbol
$\|ii'\|$	distance between node i and neighbouring node i' [m]

1. Introduction

Because of the large number of particles involved, an affordable approach to calculate industrial gas–solid flows is the Eulerian–Eulerian approach. The gas and the solid phase are described as fully interpenetrating continua [2]. The resulting set of partial differential equations is difficult to solve, due to the disperse characteristic speeds and due to the action of drag and gravity, appearing as source terms in the equations.

Most two-phase flow research groups use a sequential solver, also called pressure based algorithm [1,8,16,25], originally extended to multi-phase flows by Harlow and Amsden [14].

Simultaneous or density based solution algorithms were for single phase flow originally developed for high-Mach applications. The introduction of preconditioning [29,34], made simultaneous solvers also efficient for low-Mach single phase flow calculations.

De Wilde et al. [4] developed a semi-implicit point wise simultaneous solution algorithm for steady and unsteady gas–solid flows, with a dual-time stepping technique and preconditioning in pseudo-time. The discretization was based on an extension of the preconditioned advection upstream splitting method (AUSMP) [17,18] to multi-phase flows [4,9,10,19,21]. The semi-implicit point solver was seen to be stable in 3D calculations of gas–solid flows on low aspect ratio grids [4,5]. On higher grid aspect ratio grids, however, convergence was seen to slow down because stiffness is introduced by the numerically anisotropic behaviour of the diffusive and the acoustic terms [32].

The purpose of this paper is to present a semi-implicit plane solver and analyze the stability and convergence behaviour of the semi-implicit point and plane wise simultaneous solution algorithms for gas–solid flow at both low and high aspect ratio grids. The numerical schemes are analyzed in 2D with the Fourier method. The convergence behaviour is illustrated with 3D calculations of low speed developing gas–solid flow in a riser.

A low-Mach limit of the AUSM scheme is presented and studied. The role of the preconditioner, the discretization and the treatment of the source terms are discussed. The influence of the solids volume fraction and the gas–solid slip velocity on the numerical stability is investigated. A grid independency study is carried out, allowing to investigate the effect of grid refinement on the numerical solution and on the convergence behaviour of the simultaneous solution algorithms. Finally, the gas–solid flow model is experimentally validated.

2. Gas–solid flow model

The Eulerian–Eulerian approach is used. Table 1 summarizes the transport equations involved. The basic equation set expresses the conservation of mass, momentum and energy for each phase. For the solid phase, the transport equations are obtained via the kinetic theory of granular flow (KTGF) [12], requiring the solution of an extra transport equation for the granular temperature – a measure for the fluctuating motion of the solid phase on the single solid particle level. The KTGF is analogous to the kinetic theory of gasses but allows non-elastic particle–particle collisions [15,20]. The latter result in dissipation of granular temperature. Because the gas and solid phase temperature (≠granular temperature) are assumed to be equal, a solid phase total energy equation is not taken into account. In the present work, the commonly used model B [6,12] is applied, locating the gas phase pressure gradient entirely in the gas phase.

Because the computationally affordable mesh in gas–solid flow calculations is usually too coarse to explicitly calculate the turbulent motion, Reynolds-averaged equations are used and the turbulence is accounted for via a turbulence model. The effect of gas phase turbulence is taken into account via a

Table 1
Conservation equations

Gas phase total mass balance

$$\frac{\partial}{\partial t}\left(\varepsilon_{\mathrm{g}}\rho_{\mathrm{g}}\right)+\frac{\partial}{\partial \bar{r}}\cdot\left(\varepsilon_{\mathrm{g}}\rho_{\mathrm{g}}\bar{u}\right)=0 \tag{1}$$

Solid phase total mass balance

$$\frac{\partial}{\partial t}\left(\varepsilon_{\mathrm{s}}\rho_{\mathrm{sp}}\right)+\frac{\partial}{\partial \bar{r}}\cdot\left(\varepsilon_{\mathrm{s}}\rho_{\mathrm{sp}}\bar{v}\right)=0 \tag{2}$$

Momentum conservation gas phase

$$\frac{\partial}{\partial t}\left(\varepsilon_{\mathrm{g}}\rho_{\mathrm{g}}\bar{u}\right)+\frac{\partial}{\partial \bar{r}}\cdot\left(\varepsilon_{\mathrm{g}}\rho_{\mathrm{g}}\bar{u}\bar{u}\right)=-\frac{\partial}{\partial \bar{r}}\left(P+\frac{2}{3}\rho_{\mathrm{g}}k\right)-\frac{\partial}{\partial \bar{r}}\cdot\left(\varepsilon_{\mathrm{g}}\bar{\bar{s}}_{\mathrm{g}}\right)-\beta(\bar{u}-\bar{v})+\varepsilon_{\mathrm{g}}\rho_{\mathrm{g}}\bar{g} \tag{3}$$

where

$$\bar{\bar{s}}_{\mathrm{g}}=-\left[\left(\xi_{\mathrm{g}}-\frac{2}{3}\mu_{\mathrm{g}}\right)\left(\frac{\partial}{\partial \bar{r}}\cdot\bar{u}\right)\bar{\bar{I}}+\left(\mu_{\mathrm{g}}+\mu_{\mathrm{g}}^{t}\right)\left(\left(\frac{\partial}{\partial \bar{r}}\bar{u}\right)+\left(\frac{\partial}{\partial \bar{r}}\bar{u}\right)^{\mathrm{T}}\right)\right] \tag{4}$$

Momentum conservation solid phase

$$\frac{\partial}{\partial t}\left(\varepsilon_{\mathrm{s}}\rho_{\mathrm{sp}}\bar{v}\right)+\frac{\partial}{\partial \bar{r}}\cdot\left(\varepsilon_{\mathrm{s}}\rho_{\mathrm{sp}}\bar{v}\bar{v}\right)=-\frac{\partial}{\partial \bar{r}}P_{\mathrm{s}}-\frac{\partial}{\partial \bar{r}}\cdot\left(\varepsilon_{\mathrm{s}}\bar{\bar{s}}_{\mathrm{s}}\right)+\beta(\bar{u}-\bar{v})+\varepsilon_{\mathrm{s}}\rho_{\mathrm{sp}}\bar{g} \tag{5}$$

where

$$\bar{\bar{s}}_{\mathrm{s}}=-\left[\left(\xi_{\mathrm{s}}-\frac{2}{3}\mu_{\mathrm{s}}\right)\left(\frac{\partial}{\partial \bar{r}}\cdot\bar{v}\right)\bar{\bar{I}}+\left(\mu_{\mathrm{s}}\right)\left(\left(\frac{\partial}{\partial \bar{r}}\bar{v}\right)+\left(\frac{\partial}{\partial \bar{r}}\bar{v}\right)^{\mathrm{T}}\right)\right] \tag{6}$$

Total energy conservation equation gas phase

$$\begin{aligned}&\frac{\partial}{\partial t}\left(\varepsilon_{\mathrm{g}}\rho_{\mathrm{g}}\left(e_{\mathrm{g}}+k+q_{\mathrm{g}}\right)\right)+\frac{\partial}{\partial \bar{r}}\cdot\left(\varepsilon_{\mathrm{g}}\rho_{\mathrm{g}}\bar{u}\left(e_{\mathrm{g}}+k+q_{\mathrm{g}}\right)\right)-\frac{\partial}{\partial \bar{r}}\cdot\left(\varepsilon_{\mathrm{g}}(\lambda+\lambda^{t})\frac{\partial T}{\partial \bar{r}}\right)\\&\quad=-\frac{\partial}{\partial \bar{r}}\cdot\left(\left(P+\frac{2}{3}\rho_{\mathrm{g}}k\right)\bar{u}\right)-\frac{\partial}{\partial \bar{r}}\cdot\left(\varepsilon_{\mathrm{g}}\bar{\bar{s}}_{\mathrm{g}}\cdot\bar{u}\right)-\frac{\beta}{2}\left((\bar{u}\cdot\bar{u})-(\bar{v}\cdot\bar{v})\right)+\varepsilon_{\mathrm{g}}\rho_{\mathrm{g}}\bar{g}\cdot\bar{u}\end{aligned} \tag{7}$$

Turbulence equations gas phase
k-equation

$$\frac{\partial}{\partial t}\left(\varepsilon_{\mathrm{g}}\rho_{\mathrm{g}}k\right)+\frac{\partial}{\partial \bar{r}}\cdot\left(\varepsilon_{\mathrm{g}}\rho_{\mathrm{g}}\bar{u}k\right)=\frac{\partial}{\partial \bar{r}}\cdot\left(\varepsilon_{\mathrm{g}}\frac{\mu_{\mathrm{g}}+\mu_{\mathrm{g}}^{t}}{\sigma_{k}}\frac{\partial k}{\partial \bar{r}}\right)+\left[\varepsilon_{\mathrm{g}}\mu_{\mathrm{g}}^{t}\left[\left(\frac{\partial}{\partial \bar{r}}\bar{u}\right)+\left(\frac{\partial}{\partial \bar{r}}\bar{u}\right)^{\mathrm{T}}\right]\right]:\left(\frac{\partial}{\partial \bar{r}}\bar{u}\right)-\varepsilon_{\mathrm{g}}\rho_{\mathrm{g}}\varepsilon \tag{8}$$

ε-equation

$$\frac{\partial}{\partial t}\left(\varepsilon_{\mathrm{g}}\rho_{\mathrm{g}}\varepsilon\right)+\frac{\partial}{\partial \bar{r}}\cdot\left(\varepsilon_{\mathrm{g}}\rho_{\mathrm{g}}\bar{u}\varepsilon\right)=\frac{\partial}{\partial \bar{r}}\cdot\left(\varepsilon_{\mathrm{g}}\frac{\mu_{\mathrm{g}}+\mu_{\mathrm{g}}^{t}}{\sigma_{\varepsilon}}\frac{\partial \varepsilon}{\partial \bar{r}}\right)+C_{1\varepsilon}\frac{\varepsilon}{k}\left[\varepsilon_{\mathrm{g}}\mu_{\mathrm{g}}^{t}\left[\left(\frac{\partial}{\partial \bar{r}}\bar{u}\right)+\left(\frac{\partial}{\partial \bar{r}}\bar{u}\right)^{\mathrm{T}}\right]:\left(\frac{\partial}{\partial \bar{r}}\bar{u}\right)\right]-C_{2\varepsilon}\varepsilon_{\mathrm{g}}\rho_{\mathrm{g}}\frac{\varepsilon^{2}}{k} \tag{9}$$

Transport equation for the kinetic fluctuation energy of the solid phase

$$\frac{3}{2}\left[\frac{\partial}{\partial t}\left(\varepsilon_{\mathrm{s}}\rho_{\mathrm{sp}}\Theta\right)+\frac{\partial}{\partial \bar{r}}\cdot\left(\varepsilon_{\mathrm{s}}\rho_{\mathrm{sp}}\bar{v}\Theta\right)\right]=\frac{\partial}{\partial \bar{r}}\cdot\left(\varepsilon_{\mathrm{s}}\kappa\frac{\partial}{\partial \bar{r}}\Theta\right)-\left(P_{\mathrm{s}}\bar{\bar{I}}+\varepsilon_{\mathrm{s}}\bar{\bar{s}}_{\mathrm{s}}\right):\left(\frac{\partial}{\partial \bar{r}}\bar{v}\right)-\gamma \tag{10}$$

high-Reynolds k–ε model, adapted for gas–solid interactions [4]. The solid phase Reynolds-stress terms related to meso-scale fluctuations (e.g., clusters) [1,35] are not taken into account, as no reliable solid phase turbulence model is available yet. For the numerical investigation in the present work, the latter is of minor importance.

Constitutive equations for the solid phase physical properties are derived via the KTGF and adopted from [20].

At solid bounding walls, the no-slip condition is applied for the gas phase, whereas slip is allowed for the solid phase. The high-Reynolds k–ε model used in the bulk flow for the gas phase [11] is not valid in the immediate vicinity of the wall [26]. Therefore, use is made of wall functions based on the well-known logarithmic law [15]. No accurate model to account for the presence of solid particles in the wall functions is available yet. For the solid phase, the values of the specific shear stress and the flux of pseudo-thermal energy to the wall are calculated as in [27]. With respect to total energy transport, the solid wall is assumed to be a perfect insulator.

More details on the constitutive equations and the boundary conditions are found in [4].

The inviscid gas–solid flow model equations are not necessarily well-posed [12,28]. However, it was shown that the presence of non-zero viscous terms in the gas–solid flow model (Table 1), no matter how small, results in a well-posed system (see, e.g., [28]).

3. Integration scheme

A simultaneous solution algorithm is used [4], in contrast to the for multi-phase flows frequently used sequential solvers [14,22–24]. Thus, the pressure–velocity correction loop is eliminated.

The equation set (1)–(10) (Table 1) is written in matrix formulation as:

$$\frac{\partial Q}{\partial t} = \text{spatial terms} + \text{source terms} \tag{11}$$

with Q the vector of the conservative variables.

For the integration, a dual-time stepping technique is used. A numerical stepper, the pseudo-time τ, is introduced for the solution of the non-steady-state problem:

$$\frac{\partial Q}{\partial \tau} + \frac{\partial Q}{\partial t} = \text{spatial terms} + \text{source terms}. \tag{12}$$

An iteration loop is set up in pseudo-time. To further increase the numerical stability, a fourth-order Runge–Kutta scheme is used in the pseudo-time stepping [3,4,32,33]. At convergence, the pseudo-time step term vanishes.

The equations are linearized and solved for the viscous variables, i.e., ε_s, P, v_x, v_y, v_z, u_x, u_y, u_z, T, Θ, k, and ε, instead of the conservative variables used in previous work [3,4]. This drastically simplifies the linearization of the acoustic and the viscous fluxes. Eq. (12) is reformulated as:

$$\frac{\partial Q}{\partial W} \cdot \frac{\partial W}{\partial \tau} + \frac{\partial Q}{\partial W} \cdot \frac{\partial W}{\partial t} = \text{spatial terms} + \text{source terms} \tag{13}$$

with W the vector of the viscous variables.

3.1. Preconditioning

The integration scheme suffers from stiffness when the Mach-number is low and a partially explicit approach is taken. A fully implicit approach is computationally expensive. A cheaper solution to reduce the stiffness in the stream wise direction is to apply local preconditioning [27]. Preconditioning rescales the eigenvalues of the set of equations (Table 1 and Eq. (13)) so that they become all of the same order of magnitude. The eigenvalues correspond physically to the characteristic speeds. To perform a proper rescaling of the system, the knowledge of the characteristic speeds of the model, in particular the mixture speed of sound c_m, is essential. Experimental observations by van der Schaaf et al. [30] show a remarkable gradual decrease of the mixture speed of sound with increasing solid volume fraction. Furthermore, the mixture speed of sound was observed to be frequency dependent [13]. Gregor and Rumpf [13] have shown via an eigenvalue analysis that the Eulerian–Eulerian gas–solid flow models correctly capture the complex mixture speed of sound behaviour. Furthermore, these authors present a general mixture speed of sound equation for gas–solid flows.

The preconditioner Γ of Weiss and Smith [34], extended to gas–solid flows by De Wilde et al. [4], is further generalized to account for a more general equation for the mixture speed of sound

$$\Gamma = \begin{pmatrix} \rho_{sp} & 0 & 0 & 0 & 0 & 0 & 0 & 0 & 0 & 0 & 0 & 0 \\ -\rho_g & \varepsilon_g T_1 & 0 & 0 & 0 & 0 & 0 & 0 & \varepsilon_g K_2 & 0 & 0 & 0 \\ \rho_{sp} v_x & 0 & \varepsilon_s \rho_{sp} & 0 & 0 & 0 & 0 & 0 & 0 & 0 & 0 & 0 \\ \rho_{sp} v_y & 0 & 0 & \varepsilon_s \rho_{sp} & 0 & 0 & 0 & 0 & 0 & 0 & 0 & 0 \\ \rho_{sp} v_z & 0 & 0 & 0 & \varepsilon_s \rho_{sp} & 0 & 0 & 0 & 0 & 0 & 0 & 0 \\ -\rho_g u_x & \varepsilon_g u_x T_1 & 0 & 0 & 0 & \varepsilon_g \rho_g & 0 & 0 & \varepsilon_g u_x K_2 & 0 & 0 & 0 \\ -\rho_g u_y & \varepsilon_g u_y T_1 & 0 & 0 & 0 & 0 & \varepsilon_g \rho_g & 0 & \varepsilon_g u_y K_2 & 0 & 0 & 0 \\ -\rho_g u_z & \varepsilon_g u_z T_1 & 0 & 0 & 0 & 0 & 0 & \varepsilon_g \rho_g & \varepsilon_g u_z K_2 & 0 & 0 & 0 \\ -\rho_g E_g & \varepsilon_g (([E_g + \frac{P}{\rho_g}] T_1) - 1) & 0 & 0 & 0 & \varepsilon_g \rho_g u_x & \varepsilon_g \rho_g u_y & \varepsilon_g \rho_g u_z & C_1 & 0 & \varepsilon_g \rho_g & 0 \\ \frac{3\rho_{sp}\Theta}{2} & 0 & 0 & 0 & 0 & 0 & 0 & 0 & 0 & \frac{3\varepsilon_s \rho_{sp}}{2} & 0 & 0 \\ -\rho_g k & \varepsilon_g k T_1 & 0 & 0 & 0 & 0 & 0 & 0 & \varepsilon_g k K_2 & 0 & \varepsilon_g \rho_g & 0 \\ -\rho_g \varepsilon & \varepsilon_g \varepsilon T_1 & 0 & 0 & 0 & 0 & 0 & 0 & \varepsilon_g \varepsilon K_2 & 0 & 0 & \varepsilon_g \rho_g \end{pmatrix} \tag{14}$$

where

$$K_2 = \left.\frac{\partial \rho_g}{\partial T}\right|_P = -\frac{\rho_g}{T}, \tag{15}$$

$$C_1 = \varepsilon_g \left(\left(\left[E_g + \frac{P}{\rho_g} \right] K_2 \right) + (\rho_g C_P) \right), \tag{16}$$

$$T_1 = \left(\left(\frac{1}{u_{\text{ref}}^2} \right) + \left(\frac{1}{C_P \cdot T} \right) \right), \tag{17}$$

with

$$u_{\text{ref}} = c_g \quad \text{if} \quad | \bar{u} | > c_m \tag{18}$$

and if $|\bar{u}| < c_m$:

$$u_{\text{ref}} = |\bar{u}| \cdot (c_g / c_m) + \frac{2(\mu_g + \mu_g^{\text{tur}}) \left(\frac{\alpha}{\Delta x} + \frac{\alpha}{\Delta y} + \frac{1}{\Delta z} \right)}{\rho_g} \tag{19}$$

with $\alpha = 1$ for the semi-implicit point solver and $\alpha = 0$ for the semi-implicit plane solver (explained further in this paper) and with c_g the gas phase speed of sound and c_m the mixture speed of sound, e.g., [13].

The preconditioner depends on the mixture speed of sound c_m. As will be demonstrated, the damping characteristics and the convergence behaviour of the preconditioned dual-time stepping integration scheme strongly depend on a proper rescaling of the eigenvalues of the set of equations (Table 1 and Eq. (13)) by the preconditioner. If the preconditioner is properly scaled, the pseudo-time step can be scaled according to all characteristic speeds and convergence is fast. On the other hand, if the preconditioner is not properly scaled, the pseudo-time step is to be scaled according to the largest characteristic speed and convergence is poor.

The optimal formulation for the mixture speed of sound to be used in Eq. (19) requires some further research.

Because the pseudo-time derivative term is pre-multiplied with the preconditioner,

$$\Gamma \frac{\partial W}{\partial \tau} + \frac{\partial Q}{\partial W} \cdot \frac{\partial W}{\partial t} = \text{spatial terms} + \text{source terms} \tag{20}$$

the preconditioner affects the convergence behaviour only and not the solution.

3.2. Discretization

First-order backward discretization in physical and pseudo-time is performed:

$$\left(\frac{\Delta t}{\Delta \tau} \Gamma + \left(\frac{\partial Q}{\partial W} \right)^{(n)} \right) \cdot \left(W_i^{(t+\Delta t)^{(n+1)}} - W_i^{(t+\Delta t)^{(n)}} \right) = \left(-Q_i^{(t+\Delta t)^{(n)}} + Q_i^{(t)} \right) + (\Delta t \cdot \text{spatial terms})^{(n)} + (\Delta t \cdot \text{source terms})^{(n)}. \tag{21}$$

Eq. (21) is written for node i and taking a fully explicit approach for the spatial and source terms. The iteration number n is directly related to the pseudo-time step $\Delta\tau$.

Applying the finite volume technique results in a flux formulation of the spatial terms [4]. The discretization of the latter depends on the nature of the fluxes.

The inviscid fluxes are treated following an extension of the advection upstream splitting method (AUSM) [17,18] from single phase to multiphase flows [4,9,10,19,21]. In the present work, a simplified AUSM scheme, based on the low-Mach limit of the original AUSM-scheme, is introduced.

AUSM is based on a separate treatment of the convective and acoustic terms for each phase. Convective flux terms are treated upwind following the value of the advective velocity at the cell interface:

$$\left[\overline{\phi^{(c)}_{\mathrm{g/s}}} \cdot \bar{n} \right]_{ii'} = \phi^{\mathrm{g/s}}_{i/i'} \left(\overline{s^{\mathrm{g/s}}} \cdot \bar{n} \right)_{ii'} = \phi^{\mathrm{g/s}}_{i/i'} s^{\mathrm{g/s}}_{n_{ii'}} \tag{22}$$

with

$$\phi_{i/i'} = \begin{matrix} \phi_i \\ \phi_{i'} \end{matrix} \quad \text{if} \quad \begin{matrix} s_{n_{ii'}} \geqslant 0, \\ s_{n_{ii'}} < 0, \end{matrix} \tag{23}$$

where $s_{n_{ii'}}$ being the component of the cell interface velocity normal to the cell interface.

In the original AUSM scheme, the velocity s at the cell interface ii' combines information from wave speeds travelling towards the cell interface from the adjacent cells [4,17]. In the low-Mach limit this formulation reduces to a central scheme:

$$s_{ii'} = \frac{s_i + s_{i'}}{2}. \tag{24}$$

The acoustic flux terms are governed by the acoustic wave speeds and in the low-Mach limit the pressure splitting reduces to a central scheme:

$$P_{ii'} = \frac{P_i + P_{i'}}{2}. \tag{25}$$

To improve the pressure–velocity coupling and the numerical stability, artificial dissipation is to be added [4,18]. Following [33], artificial dissipation should be added to the mass flux in all equations. Artificial dissipation is added to all gas phase equations in the present work, in contrast to previous work [4] where artificial dissipation is only added to the gas phase mass and total energy equations. No artificial dissipation is added to the solid phase equations, as the gas phase pressure gradient is distributed entirely over the gas phase (model B) [12].

For the gas phase mass balance Eq. (1), the artificial dissipation term at each cell interface ii' is proportional to

$$\delta_{\mathrm{ad}} \frac{(P_{i'} - P_i)}{\beta_n} \tag{26}$$

in which δ_{ad} is the artificial dissipation parameter with a typical value of about 0.5;

$$\beta_n = |\overline{u_{\max}}| + \frac{2(\mu_{g_{ii'}} + \mu^{\mathrm{tur}}_{g_{ii'}})}{\rho_{g_{ii'}} \cdot |ii'|} \tag{27}$$

with: $|\overline{u_{\max}}|$ the maximum convective speed in the flow field.

β_n (Eq. (27)) consists of a convective and viscous contribution, respectively. In Eq. (27), $|ii'|$ is the distance between node i and neighbouring node i'.

For the other equations, the mass balance artificial dissipation term is to be multiplied with the transported viscous variable. Remark that Eq. (26) contains no pressure gradient, but a pressure difference. As a result, for infinitely fine meshes, the artificial dissipation terms vanish.

The viscous fluxes are calculated following a central scheme [3].

Applying the different splitting techniques, the spatial terms in Eq. (21) can be formally written in terms of contributions of node i, neighbouring nodes i' and non-neighbouring nodes i'':

$$\left(\frac{\Delta t}{\Delta \tau}\Gamma + \left(\frac{\partial Q}{\partial W}\right)^{(n)}\right) \cdot \left(W_i^{(t+\Delta t)^{(n+1)}} - W_i^{(t+\Delta t)^{(n)}}\right) = \left(-Q_i^{(t+\Delta t)^{(n)}} + Q_i^{(t)}\right) + \left(\Delta t \cdot F(i,i',i'')\right)^{(n)} + \left(\Delta t \cdot \text{source terms}\right)^{(n)}, \tag{28}$$

where F is a summation of convective, acoustic and viscous fluxes:

$$F = F^{(c)} + F^{(a)} + F^{(v)}. \tag{29}$$

An explicit, semi-implicit, or fully implicit treatment of some or all of the spatial terms can be chosen. An implicit treatment with respect to information from node i requires the calculation of the Jacobian of the flux vector with respect to the variables of node i:

$$F(i,i',i'')^{(i:n+1)} = F(i,i',i'')^{(i:n)} + \left(\frac{\partial F(i,i',i'')}{\partial W_i}\right)^{(n)} \cdot \left(W_i^{(n+1)} - W_i^{(n)}\right). \tag{30}$$

An implicit treatment with respect to node i and some or all of the neighbouring nodes i' also requires the calculation of the Jacobian of the flux vector with respect to the variables of neighbouring nodes i' and results in:

$$F(i,i',i'')^{(i,i':n+1)} = F(i,i',i'')^{(i,i':n)} + \left(\frac{\partial F(i,i',i'')}{\partial W_i}\right)^{(n)} \cdot \left(W_i^{(n+1)} - W_i^{(n)}\right) + \left(\frac{\partial F(i,i',i'')}{\partial W_{i'}}\right)^{(n)} \cdot \left(W_{i'}^{(n+1)} - W_{i'}^{(n)}\right). \tag{31}$$

The last term in Eq. (30) or the two last terms in Eq. (31) are transferred to the left-hand side of Eq. (28). In case Eq. (31) is used, Eq. (28) is transformed into:

$$\left[\frac{\Delta t}{\Delta \tau}\Gamma + \left(\frac{\partial Q}{\partial W}\right)^{(n)} - \left(\frac{\partial F(i,i',i'')}{\partial W_i}\right)^{(n)}\right] \cdot \left(W_i^{(t+\Delta t)^{(n+1)}} - W_i^{(t+\Delta t)^{(n)}}\right) - \left(\frac{\partial F(i,i',i'')}{\partial W_{i'}}\right)^{(n)} \cdot \left(W_{i'}^{(t+\Delta t)^{(n+1)}} - W_{i'}^{(t+\Delta t)^{(n)}}\right) = \left(-Q_i^{(t+\Delta t)^{(n)}} + Q_i^{(t)}\right) + \left(\Delta t \cdot F(i,i',i'')^{(n)}\right) + \left(\Delta t \cdot \text{source terms}\right)^{(n)}. \tag{32}$$

Eq. (32) can be rewritten as:

$$A_{i,i}^{(n)} \cdot \Delta W_i - A_{i,i'}^{(n)} \cdot \Delta W_{i'} = \left(Q_i^{(t)} - Q_i^{(t+\Delta t)^{(n)}} \right) + \left(\Delta t \cdot F(i, i', i'')^{(n)} \right) + (\Delta t \cdot \text{source terms})^{(n)} \tag{33}$$

introducing the square matrices $A_{i,i}^{(n)}$ and $A_{i,i'}^{(n)}$ with a dimension equal to the number of equations. These matrices are used in the general matrix formulation for all nodes presented next.

3.3. Treatment of the source terms

Source terms occur in the conservation equations (Table 1) as a result of gravity and gas–solid interactions. Furthermore, the granular temperature equation and the turbulence transport equations contain dissipation and production terms [7].

Following [7], De Wilde et al. [4] split all source terms into a positive and a negative part. Only the negative part is treated implicitly. In the present work, a fully explicit and a fully implicit treatment of the gravity and drag source terms are also tested to investigate the effect on the numerical stability. The possibility of a fully implicit treatment of the source terms is a particular advantage of the simultaneous solution algorithms. With a sequential solution algorithm, only a semi-implicit treatment with respect to one of the variables is possible.

Remark that for the turbulence source terms, the negative part only is treated implicitly. Such an approach was shown to be optimal [7] and the treatment of the turbulence source terms is adopted from [7] and is not further investigated in the present work. The drag and gravity source terms are focused on.

For a fully implicit treatment of the source terms the source terms K are, after linearization, taken into account as:

$$K^{(n+1)} = K^{(n)} + \left(\frac{\partial K}{\partial W} \right)^{(n)} \cdot \left(W^{(n+1)} - W^{(n)} \right) = K^{(n)} + \left(\frac{\partial K}{\partial W} \right)^{(n)} \cdot \Delta W. \tag{34}$$

This formulation is included in Eq. (32).

3.4. Simultaneous solution algorithms: point and plane solver

Eq. (33) written down for all nodes i can be expressed in matrix formulation, for example:

$$\begin{pmatrix} A_{1,1} & \ldots 0 \ldots & A_{1,i'_1} & \ldots 0 \ldots & A_{1,i'_2} & \ldots \\ \ldots & A_{2,2} & \ldots 0 \ldots & A_{2,i'_1} & A_{2,i'_2} & \ldots \\ & & \ddots & & & \\ A_{i,i'_1} & \ldots 0 \ldots & A_{i,i'_2} & A_{i,i} & \ldots & \\ & & & & \ddots & \\ & \ldots & A_{nn,i'_1} & & \ldots 0 \ldots & A_{nn,nn} \end{pmatrix} \cdot \begin{pmatrix} \Delta W_1 \\ \Delta W_2 \\ \vdots \\ \Delta W_i \\ \vdots \\ \Delta W_{nn} \end{pmatrix} = \begin{pmatrix} B_1 \\ B_2 \\ \vdots \\ B_i \\ \vdots \\ B_{nn} \end{pmatrix} \tag{35}$$

or

$$A \cdot \Delta W = B, \tag{36}$$

where ΔW_i and B_i are vectors of dimension equal to the number of equations, as defined by Eqs. (32) and (33), and nn is the number of nodes.

Matrix A in Eqs. (35) and (36) is sparse. In case an explicit or a semi-implicit point solver is used, only the diagonal elements $A_{i,\ i}$ will contain non-zero elements. In that case, the equations can be solved point wise with the Jacobi method [4]. If a semi-implicit plane solver is applied, the off-diagonal elements $A_{i,i'}$ corresponding to the interaction terms of a node i with the neighbouring nodes i' in the considered plane will contain non-zero elements as well. This requires the simultaneous solution of all nodes in the plane. Hence, matrix A (Eqs. (35) and (36)) can be rewritten in a block structure. The nodes in a block are solved simultaneously, whereas the different blocks can be solved independently. Remark that a 2D plane in a 3D simulation corresponds to a 1D line in a 2D simulation.

Most risers have a high aspect ratio, i.e., the diameter of a riser is much smaller than its length. Therefore, for the numerical solution, high grid aspect ratios are commonly used, with the smallest distance between the nodes in the directions perpendicular to the axis of the riser, i.e., perpendicular to the main flow direction. Hence, numerical stability restrictions are the most strict in the directions perpendicular to the axis of the riser. By choosing the cross sections perpendicular to the axis of the riser to be solved plane wise, i.e., by handling the interactions between all nodes in each of these cross sections of the riser in an implicit way and solving these nodes simultaneously, the strict stability restrictions in these plane directions are eliminated.

For a semi-implicit point solver, the pseudo-time step introduced in Eq. (12) is restricted following the 3D Courant–Friedrichs–Lewy (CFL) condition:

$$\left(\frac{u_x+\tilde{c}}{\Delta x}+\frac{u_y+\tilde{c}}{\Delta y}+\frac{u_z+\tilde{c}}{\Delta z}\right)\cdot\Delta\tau=\mathrm{CFL}\approx 1, \tag{37}$$

where $\tilde{c}$ is the numerical speed of sound as obtained by the use of preconditioning (Eqs. (14)–(20)).

For a semi-implicit plane solver, with the plane in the x and y directions, the pseudo-time step is only restricted by

$$\left(\frac{u_z+\tilde{c}}{\Delta z}\right)\cdot\Delta\tau=\mathrm{CFL}\approx 1, \tag{38}$$

z being the direction of the riser axis.

Thus, a plane solver allows the use of a much larger pseudo-time step for the calculations and, as a result, reduces the number of iterations. The same argumentation holds for the Neumann condition for viscous effects [32].

The equation set corresponding to a plane

$$A_l\cdot\Delta W_l=B_l \tag{39}$$

is solved by a sparse direct solver. Interactions between planes and non-linearities are solved during pseudo-time stepping.

4. Stability analysis of the numerical scheme

The presented numerical schemes are analyzed using a Fourier analysis [32]. A 2D rectangular grid without stretching and with periodical boundary conditions is assumed. The grid and the related notations used are explained in Fig. 1.

Assuming a positive value for the x and y components of the velocities, the equations for the semi-implicit point solver are given by

$$\begin{aligned}&\left(\frac{\Gamma}{\Delta\tau}+A_c+B_c+A_a+B_a+2(A_v+B_v)+2(A_d+B_d)\right)\left(W^{(n+1)}-W^{(n)}\right)-A_a\frac{\left(W^{(n)}_{i+1,j}-W^{(n)}_{i-1,j}\right)}{2}\\&\quad-B_a\frac{\left(W^{(n)}_{i,j+1}-W^{(n)}_{i,j-1}\right)}{2}-A_c\left(W^{(n)}_{i,j}-W^{(n)}_{i-1,j}\right)-B_c\left(W^{(n)}_{i,j}-W^{(n)}_{i,j-1}\right)-(A_v+A_d)\left(W^{(n)}_{i-1,j}-2W^{(n)}_{i,j}+W^{(n)}_{i+1,j}\right)\\&\quad-(B_v+B_d)\left(W^{(n)}_{i,j-1}-2W^{(n)}_{i,j}+W^{(n)}_{i,j+1}\right)-f_v\left(W^{(n)}_{i-1,j-1},W^{(n)}_{i-1,j+1},W^{(n)}_{i+1,j-1},W^{(n)}_{i+1,j+1}\right)=D+G.\end{aligned} \tag{40}$$

For the definition of A_c, B_c, A_a, B_a, A_v, B_v, A_d, and B_d, reference is made to Appendix A. The source terms consist of the drag (D) and gravity (G). The treatment of the turbulence source terms and the effect on the numerical stability was analyzed by [7] and the turbulence source terms are not further considered for the stability analysis in this paper.

Assuming a positive value for the x and y components of the velocities, the equations for the semi-implicit plane solver are given by

$$\begin{aligned}&\left(\frac{\Gamma}{\Delta\tau}+A_c+A_a+2A_v+2A_d\right)\left(W^{(n+1)}-W^{(n)}\right)-A_a\frac{\left(W^{(n)}_{i+1,j}-W^{(n)}_{i-1,j}\right)}{2}-B_a\frac{\left(W^{(n+1)}_{i,j+1}-W^{(n+1)}_{i,j-1}\right)}{2}\\&\quad-A_c\left(W^{(n)}_{i,j}-W^{(n)}_{i-1,j}\right)-B_c\left(W^{(n+1)}_{i,j}-W^{(n+1)}_{i,j-1}\right)-(A_v+A_d)\left(W^{(n)}_{i-1,j}-2W^{(n)}_{i,j}+W^{(n)}_{i+1,j}\right)\\&\quad-(B_v+B_d)\left(W^{(n+1)}_{i,j-1}-2W^{(n+1)}_{i,j}+W^{(n+1)}_{i,j+1}\right)-f_v\left(W^{(n)}_{i-1,j-1},W^{(n)}_{i-1,j+1},W^{(n)}_{i+1,j-1},W^{(n)}_{i+1,j+1}\right)=D+G.\end{aligned}\tag{41}$$

For the definition of A_c, B_c, A_a, B_a, A_v, B_v, A_d, and B_d, reference is made to Appendix A.

4.1. Fourier analysis

In general, the state of variables Q can be written as the sum of the solution $\langle Q\rangle$ and an error Ψ which is function of the pseudo time τ:

$$Q(x,y,\tau)=\langle Q\rangle(x,y)+\Psi(x,y,\tau).\tag{42}$$

The error can be written as a sum of Fourier waves. The Fourier component, with wave number ω_x in the x direction and wave number ω_y in the y direction, is written as:

$$\Psi_{\omega_x,\omega_y}(x,y,\tau)=\phi(\tau)\,\mathrm{e}^{\mathrm{j}\left(\omega_x x+\omega_y y\right)},\tag{43}$$

where j represents the imaginary unit. Substitution of Eq. (43) into the set of equations describing the discretised hydrodynamic model (Eqs. (1)–(10)) results in a set of equations for the error. The linear terms are transferred into identical expressions. The non-linear terms need some explanation.

As an example, the error due to the quadratic term $\partial u^2/\partial x$ is developed, with u one of the components of the gas phase velocity vector $\bar{u}$. Using the upwind formulation (Eqs. (22) and (23)) and assuming a positive velocity component u, the first-order discretization of this term is written as:

$$\frac{1}{\mathrm{d}x}\left(u_{i+1/2}u_i-u_{i-1/2}u_{i-1}\right).\tag{44}$$

For the non-linear terms, a uniform flow field is assumed. Then u can be written as

$$u_k=\langle u\rangle+\Psi_k,\tag{45}$$

where k stands for any subscript and $\langle\rangle$ indicates the mean constant value in the flow field of, in this case, a component of the gas phase velocity. Using this expression, Eq. (44) becomes:

$$\frac{1}{\mathrm{d}x}\langle u\rangle\left(\Psi_{i+1/2}-\Psi_{i-1/2}+\Psi_i-\Psi_{i-1}+\mathrm{O}\left(\Psi^2\right)\right).\tag{46}$$

By introducing Eq. (43), the coefficient of the term $\mathrm{e}^{\mathrm{j}(\omega_x x+\omega_y y)}$ can be written as:

$$\phi(\tau)\langle u\rangle(ce(\theta_x,\mathrm{d}x)+up(\theta_x,\mathrm{d}x)),\tag{47}$$

where $ce()$ results from the central discretization scheme (Eq. (24)):

$$ce(\theta,\mathrm{d}s)=0.5\cdot\left(\mathrm{e}^{\mathrm{j}\cdot\theta}-\mathrm{e}^{-\mathrm{j}\cdot\theta}\right)\cdot\mathrm{d}s^{-1}\tag{48}$$

and *up*() results from the upwind discretization scheme. For the first-order upwind scheme (Eq. (23)):

$$up(\theta, \mathrm{d}s) = \left(1 - \mathrm{e}^{-\mathrm{j}\cdot\theta}\right) \cdot \mathrm{d}s^{-1}, \tag{49}$$

with $\theta = \omega \cdot \mathrm{d}s$, ω being the wave number and d*s* a spatial dimension.

Similar equations hold if the velocity component u is negative.

An analogous approach is taken for combination terms. As an example, when using the upwind formulation Eqs. (22) and (23) and assuming positive v, $\partial(\varepsilon_s \cdot \rho_{\mathrm{sp}} \cdot v)/\partial x$ becomes:

$$\frac{1}{\mathrm{d}x}\left(\varepsilon_{\mathrm{s}_i}\rho_{\mathrm{sp}_i}v_{i+1/2} - \varepsilon_{\mathrm{s}_{i-1}}\rho_{\mathrm{sp}_{i-1}}v_{i-1/2}\right). \tag{50}$$

Assuming a uniform flow field for the non-linear terms and introducing a perturbation results in the following expression for the coefficient of the term $\mathrm{e}^{\mathrm{j}\left(\omega_x x + \omega_y y\right)}$:

$$\phi(t)\left(\left\langle\varepsilon_{\mathrm{s}} \cdot \rho_{\mathrm{sp}}\right\rangle \cdot ce(\theta_x, \mathrm{d}x) + \left\langle\rho_{\mathrm{sp}} \cdot v\right\rangle \cdot up(\theta_x, \mathrm{d}x)\right), \tag{51}$$

where ⟨⟩ again indicates the mean constant value of the flow field.

For completeness, $vi(\theta, \mathrm{d}s)$ and $vi2(\theta, \theta b, \mathrm{d}s1, \mathrm{d}s2)$ are given, because they are needed for the viscous contributions and the artificial dissipation terms:

$$vi(\theta, \mathrm{d}s) = \left[\left(-\mathrm{e}^{-\mathrm{j}\cdot\theta} + 2\right) - \mathrm{e}^{\mathrm{j}\cdot\theta}\right] \cdot \mathrm{d}s^{-2} \tag{52}$$

and

$$vi2(\theta, \theta b, \mathrm{d}s1, \mathrm{d}s2) = \left[\left(-\mathrm{e}^{-\mathrm{j}\cdot\theta}\right) + \mathrm{e}^{\mathrm{j}\cdot\theta b} + \mathrm{e}^{-\mathrm{j}\cdot\theta b} - \mathrm{e}^{\mathrm{j}\cdot\theta}\right] \cdot 0.25 \cdot \mathrm{d}s1^{-1} \cdot \mathrm{d}s2^{-1} \tag{53}$$

with d*s*1 and d*s*2 two spatial dimensions.

Neglecting higher-order terms in the error component, the following set of algebraic equations for the error has to be solved for each stage in the pseudo-time-marching procedure:

$$\hat{P}\Delta\Psi + \hat{C}\Psi = 0 \Rightarrow \Delta\Psi = -\hat{P}^{-1}\hat{C}\Psi. \tag{54}$$

The Fourier matrix $\Im(\theta_x, \theta_y)$ is then given by

$$\Im\left(\theta_x, \theta_y\right) = -\mathrm{CFL} \cdot \hat{P}\left(\theta_x, \theta_y\right)^{-1}\hat{C}\left(\theta_x, \theta_y\right). \tag{55}$$

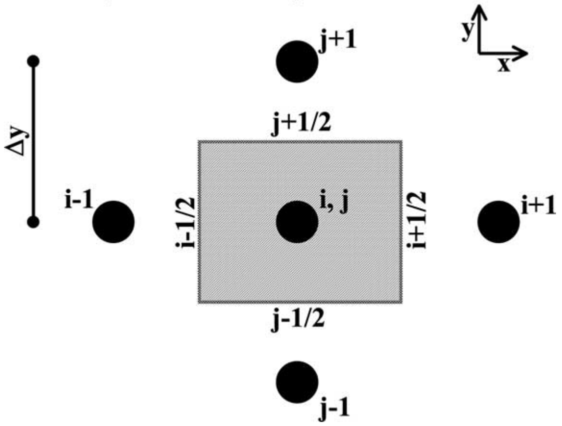

Fig. 1. 2D cell-centered mesh.

The Fourier symbol is defined as the eigenvalues of the Fourier matrix. As the pseudo-time stepping is coupled to a fourth-order Runge–Kutta method in the integration algorithm, the eigenvalues to be determined are:

$$\lambda(\theta_x,\theta_y) = \text{eigenvalues}\Big(\bar{\bar{I}} + a_4\cdot\Im(\theta_x,\theta_y)\cdot\Big(\bar{\bar{I}} + a_3\cdot\Im(\theta_x,\theta_y)\cdot\Big(\bar{\bar{I}} + a_2\cdot\Im(\theta_x,\theta_y)\cdot\Big(\bar{\bar{I}} + a_1\cdot\Im(\theta_x,\theta_y)\Big)\Big)\Big)\Big) \tag{56}$$

with $a_1 = 1/4$, $a_2 = 1/3$, $a_3 = 1/2$, and $a_4 = 1$.

The amplification factor is defined as the maximum absolute value of the eigenvalues determined by Eq. (56).

The expressions for $\hat{P}$ in Eqs. (54) and (55) depend on the time-stepping method that is used and are given below. The expression for $\hat{C}$ in Eqs. (54) and (55) is given by

$$\hat{C} = \hat{A} + \hat{B} + D_\mathrm{R} + G_\mathrm{R}, \tag{57}$$

where $\hat{A}$ contains in the x direction, respectively, the convective term $\hat{A}_\mathrm{c}$, the acoustic term $\hat{A}_\mathrm{a}$, the diffusion term $\hat{A}_\mathrm{v}$, and the artificial dissipation term $\hat{A}_\mathrm{d}$, and $\hat{B}$ contains the corresponding terms in the y direction:

$$\hat{A} = \hat{A}_\mathrm{c} + \hat{A}_\mathrm{a} + \hat{A}_\mathrm{v} + \hat{A}_\mathrm{d}, \tag{58}$$

$$\hat{B} = \hat{B}_\mathrm{c} + \hat{B}_\mathrm{a} + \hat{B}_\mathrm{v} + \hat{B}_\mathrm{d}, \tag{59}$$

D_R and G_R represent the contribution from the drag and gravity source terms.

For the formulation of the different terms in Eqs. (57)–(59), reference is made to Appendix B.

For the semi-implicit point solver, $\overset{\frown}{P}$ is equal to $\overset{\frown}{\Gamma}_P$, with

$$\overset{\frown}{P} = \overset{\frown}{\Gamma}_P = \frac{\Gamma}{\Delta\tau} + A_\mathrm{c} + B_\mathrm{c} + A_\mathrm{a} + B_\mathrm{a} + 2(A_\mathrm{v} + B_\mathrm{v}) + 2(A_\mathrm{d} + B_\mathrm{d}) + D_\mathrm{L} + G_\mathrm{L}. \tag{60}$$

For the semi-implicit plane solver, $\overset{\frown}{P}$ is given by

$$\overset{\frown}{P} = \overset{\frown}{\Gamma}_\mathrm{L} + \overset{\frown}{B}_\mathrm{c} + \overset{\frown}{B}_\mathrm{a} + \overset{\frown}{B}_\mathrm{v} + \overset{\frown}{B}_\mathrm{d} + D_\mathrm{L} + G_\mathrm{L} \tag{61}$$

with $\overset{\frown}{\Gamma}_\mathrm{L}$:

$$\overset{\frown}{\Gamma}_\mathrm{L} = \frac{\Gamma}{\Delta\tau} + A_\mathrm{c} + A_\mathrm{a} + 2A_\mathrm{v} + 2A_\mathrm{d}. \tag{62}$$

Source terms can be included in an explicit, partially implicit, or fully implicit way. The corresponding expressions for D_L and G_L are given in Appendix A.

For the Fourier analysis, flow aligned with the x direction, i.e., the direction of the largest mesh spacing, is investigated. In a riser simulation, this would correspond to the vertical direction. Except when otherwise specified, the solids volume fraction is 0.05 and the gas–solid slip is 1%. In the viscous turbulent cases, the gas phase turbulent kinetic energy k is 6.0 J kg^{-1}, the gas phase turbulence dissipation ε is 20.0 m^2 s^{-3} and the granular temperature Θ is given a value of 3.5 J kg^{-1}.

5. 3D simulation test case

The stability results are compared with the convergence behaviour of 3D simulations of developing flow in a riser of 10 cm diameter and 1 m height (Fig. 2, left). By using a large physical time step (>5000 s), a steady-state solution is calculated. With respect to numerical stability, steady-state simulations are more demanding than time dependent simulations, in particular for multi-phase flows.

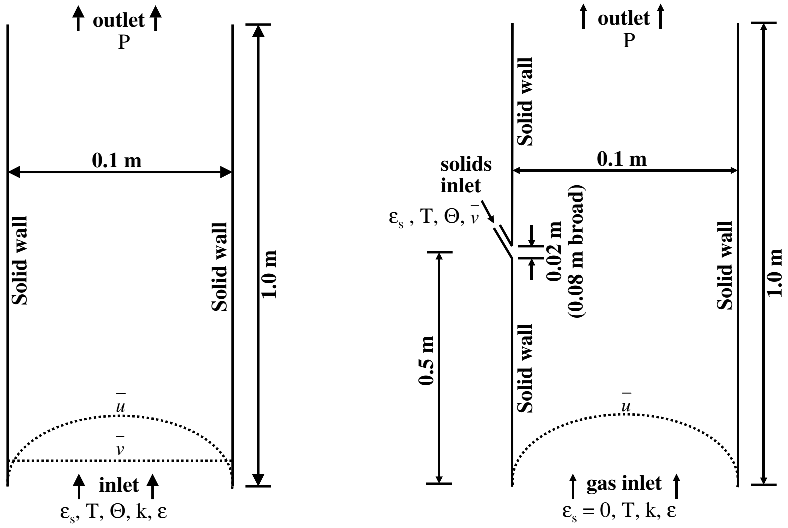

Test case Experimental validation case

Fig. 2. Geometrical configuration used for the 3D simulations.

Gas and solids are fed over the entire bottom section and a straight top outlet is used (Fig. 2, left). The solid particles have a diameter of 60 μm and a density of 1550.0 kg m^{-3} (FCC catalyst). Elastic particle–particle collisions are assumed, i.e., the restitution coefficient for particle–particle collisions [4,15] is one. The inlet solids volume fraction is 15.7%. The average gas phase inlet velocity is 12.0 m s^{-1} and a fully developed turbulent inlet velocity profile is imposed. The inlet gas phase turbulent intensity is taken 5%. The solid phase is homogeneously distributed at an inlet velocity of 4.0 m s^{-1} and the inlet granular temperature is 2.4 m^2 s^{-2}. The pressure is imposed at the outlet. The simulation conditions are summarized in Table 2 (left).

The computational mesh consists of horizontal layers which are Cartesian-radial block structured [3,4]. For the test case simulations, 73 nodes are distributed in a uniform way in each horizontal layer. Thirteen horizontal layers are distributed in a uniform way along the axis of the riser. In total, the computational

Table 2
Simulation conditions for the 3D riser simulations

Property	Value	
	Test case	Experimental validation case (side solids inlet)
$\left\langle \overline{u^{\rm in}} \right\rangle$ [m s^{-1}]	12.0	5.31
$\overline{v^{\rm in}}$ [m s^{-1}]	4.0	(0, −1.4, −0.9)
$G_{\rm s}$ [kg m^{-2} s^{-1}]	975.0	3
$\varepsilon_{\rm s}^{\rm in}$ [/]	1.572e^{-1}	5.6e^{-3}
$\Theta^{\rm in}$ [m^2 s^{-2}]	2.4	0.26
$\rho_{\rm sp}$ [kg m^{-3}]	1550.0	1550.0
$d_{\rm p}$ [μm]	60.0	77.0
e	1.0	
$e_{\rm wall}$	0.9	
ϕ	0.5	

mesh consists of 949 nodes. A grid independency study and the effect of grid refinement on the convergence behaviour of the simultaneous solution algorithms is presented further in this paper.

6. Results and discussion

Different flow situations are analyzed and a comparison is made between the results obtained with the different integration techniques. The figures show the computed eigenvalues or the Fourier symbol (Eq. (56)) in the complex plane for $\theta_x \in [0, 2\pi]$ with steps of $\Delta\theta_x = \pi/20$ and for $\theta_y = 0$, $\pi/2$, π, and $3\pi/2$. The stability domain of the fourth-order Runge–Kutta method, as combined in the integration scheme with pseudo-time stepping, together with the eigenvalues or the Fourier symbol are shown in the left panel of the figures. The amplification factors for the algorithm are shown in the right panel of the figures. For each (θ_x, θ_y) combination, the maximum modulus of the eigenvalues of the amplification matrix is shown. All Fourier symbols and stability results are computed with a CFL-number equal to 1.0. Standard, a plane solver is investigated, but the stability of point and plane solver are compared as well. For the point solver, the pseudo-time step is calculated via Eq. (37), whereas for the plane solver Eq. (38) is applied.

Unless otherwise specified, local preconditioning is applied, artificial dissipation is added with $\delta_{\mathrm{ad}} = 0.5$ and the source terms are treated fully implicit.

For the 3D test case riser simulations, convergence plots are shown. The convergence behaviour is quantified for each of the equations by determining, over all nodes, the maximum of the residual of the balance over the control volumes.

6.1. Influence of the numerical techniques

6.1.1. Preconditioning

Fig. 3 investigates the role of preconditioning on the stability of the simultaneous solution algorithms. The grid aspect ratio gar is equal to 1.0. Fig. 4 shows the corresponding convergence plots for the 3D test case riser simulation (Table 2, left and Fig. 2, left) using a CFL number equal to 1.0.

In case no preconditioning is applied, the simultaneous solution algorithms are stable, but damping is very poor and as a result convergence is slow, especially for the gas phase mass and total energy equations which play an important role in preconditioning. When applying preconditioning, on the other hand, the damping characteristics of the simultaneous solution algorithms are much improved and convergence is seen to be fast and exponential for all equations.

As is seen in the amplification factors, strong coupling in the flow direction is obtained using preconditioning: for any θ_y, good damping is assured in the θ_x direction, in particular when θ_x approaches π (Fig. 3, bottom right). The strong coupling in the flow direction is a consequence of the preconditioning, which rescales the eigenvalues in such a way that, in the flow direction, they all become of the same order of magnitude.

In the investigated case of flow aligned with the x direction, for $\theta_x = 0$, the amplification factor is equal to 1. This implies a loss of coupling for the corresponding eigenvector combination of the variables. This is often considered to be the reason for slow convergence in aligned flow. However, computations by Vierendeels et al. [32] show that this is not correct. Good performance in aligned cases results from the role of the boundary conditions. When Dirichlet boundary conditions are used, at the outlet for the pressure and at the inlet for the other variables, the strong coupling of the variables in the flow direction eliminates the unsmoothed eigenvector combination. This effect is not visible in the Fourier analysis, which applies periodic boundaries.

Remark that in aligned flow, the eigenvalues in the normal direction still have a different order of magnitude. The stiffness in the normal direction is largely removed by using a plane-implicit solver [32]. The

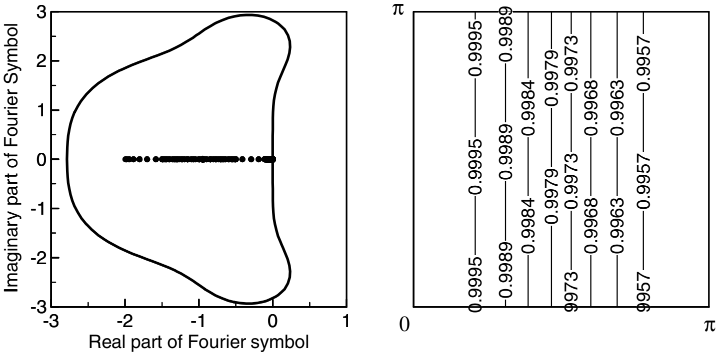

No preconditioning

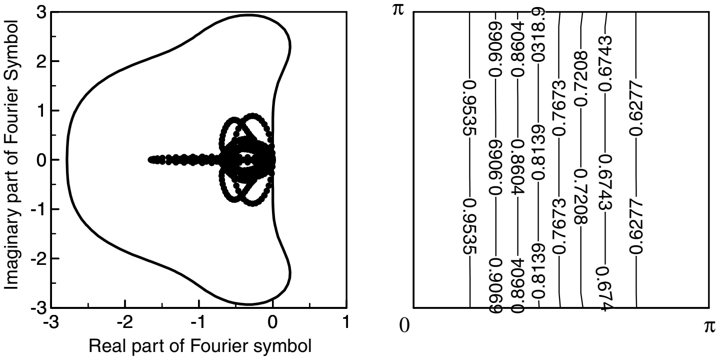

Preconditioning based on the mixture speed of sound c_m (Eqs. (14-19)).

Fig. 3. Impact of preconditioning. Stability results for turbulent viscous flow aligned with the x direction. Conditions: $\varepsilon_s = 5 \times 10^{-2}$, gar = 10.0, k = 6.0, ε = 20.0, Θ = 3.5, slip = 1%, CFL = 1.0. Integration algorithm: plane solver, artificial dissipation δ_{ad} = 0.5, implicit treatment of source terms. Left: Fourier symbols in the complex plane; right: amplification factor.

latter also guarantees convergence behaviour independent of the grid aspect ratio, as illustrated further in this paper.

It was observed that the convergence behaviour strongly depends on the correct scaling of the preconditioner. The latter requires the knowledge of the eigenvalues of the set of partial differential equations (1)–(10) (Table 1) describing gas–solid flow, in particular the mixture speed of sound. The preconditioner (Eqs. (14)–(19)) is to be scaled according to the model mixture speed of sound.

Fig. 5 shows for the 3D test case riser simulation (Table 2, left and Fig. 2, left) the calculated solids volume fraction profile (Fig. 5, left), the axial solids velocity profile (Fig. 5, middle), and the granular temperature profile (Fig. 5, right) in an axial cross section of the riser. Typically a core–annulus flow pattern develops [4,12,27]. As seen from Fig. 5 (middle), showing the axial solids velocity profiles, the acceleration zone reaches beyond the simulated first meter of the riser. This explains why the solids volume fraction (Fig. 5, left) is overall higher than the expected average value of 5% for the fully developed zone of the riser, corresponding with the imposed inlet conditions (Table 2, left). In the bottom of the riser, there is an initial zone of about 10 cm where almost no axial acceleration of the particles is seen calculated. In this zone, the radial motion is initialized. The latter is a result of the granular temperature profile that develops (Fig. 5, right). The granular temperature in the bottom region is seen to be much higher in the core than

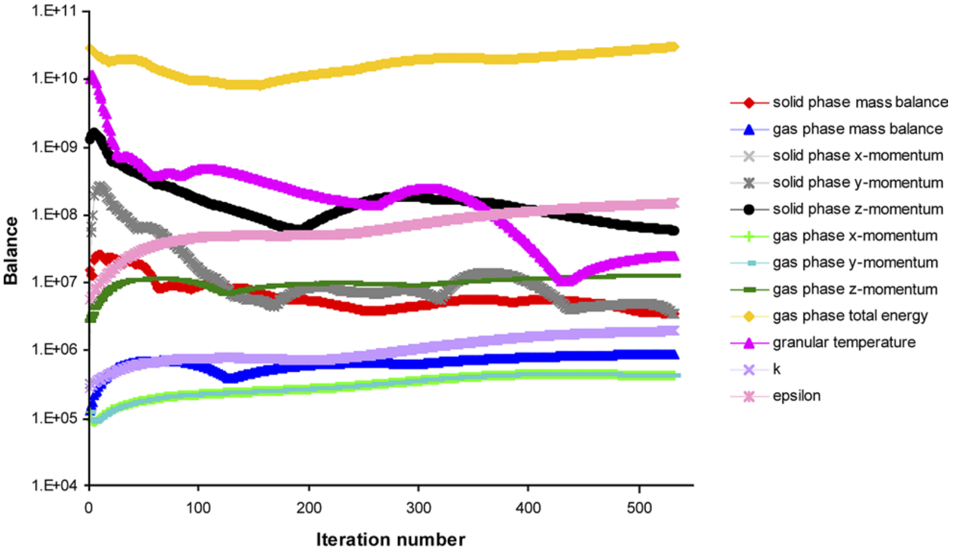

No preconditioning

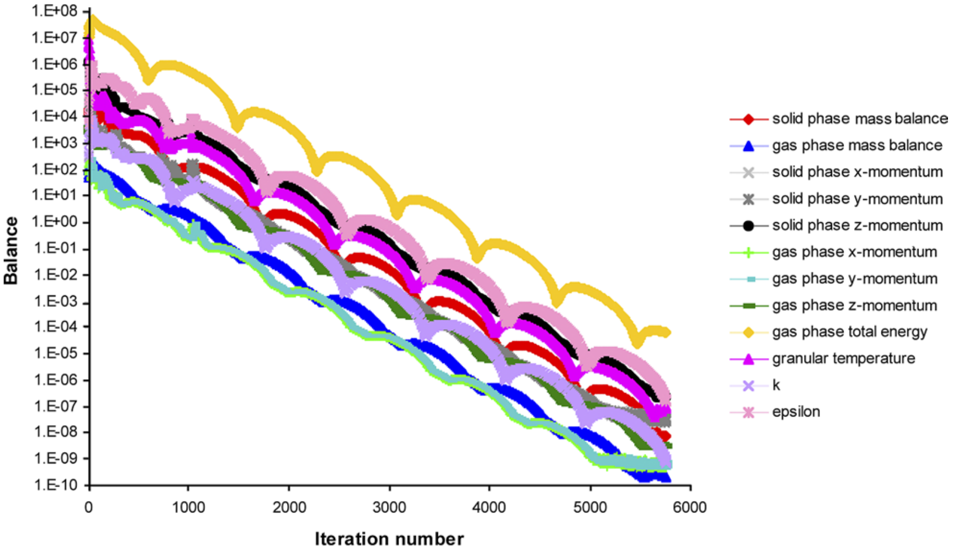

Preconditioning

Fig. 4. Impact of preconditioning. Convergence plots for 3D test case riser simulations (Table 2, left; Fig. 2, left): gar = 10, CFL = 1.0. Integration algorithm: plane solver, artificial dissipation $\delta_{\mathrm{ad}} = 0.5$, implicit treatment of source terms.

near the solid wall. This granular temperature profile is at the origin of the radial segregation of the particles and of the core–annulus flow pattern that develops. Axial acceleration of the particles starts at an elevation of about 10 cm, where a core–annulus flow pattern has developed, and is almost linear with height in most of the acceleration zone (Fig. 5, middle).

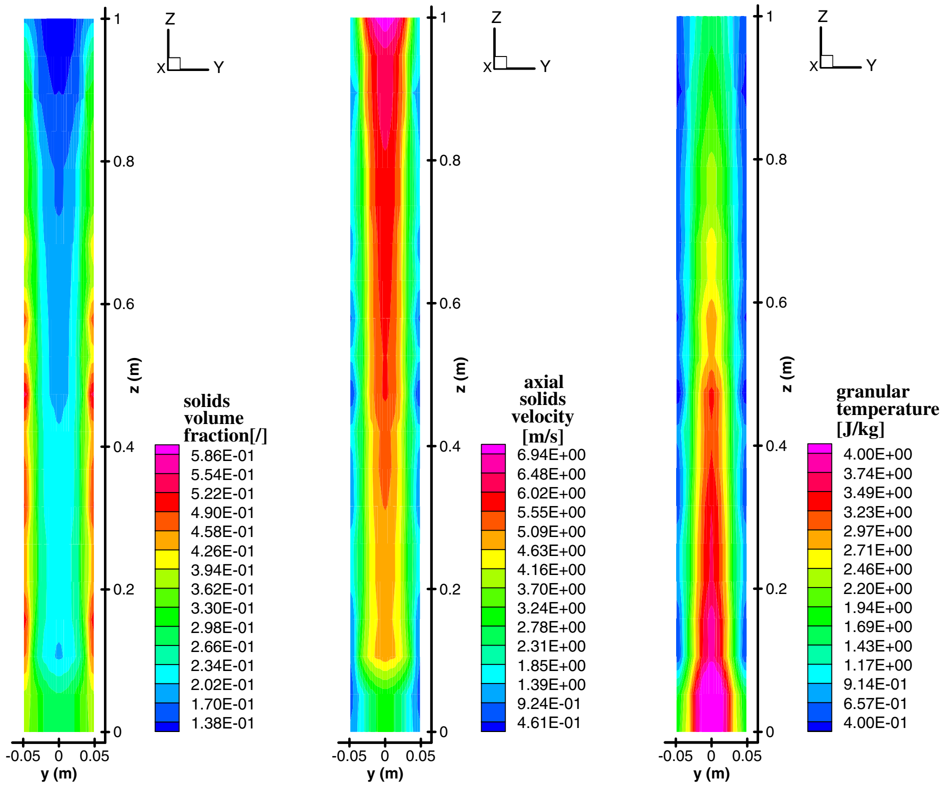

solids volume fraction axial solids velocity granular temperature

Fig. 5. Simulation results of the 3D test case riser simulation (Table 2, left; Fig. 2, left).

6.1.2. Artificial dissipation

Fig. 6 investigates the effect of artificial dissipation on the numerical stability of the integration scheme. The grid aspect ratio gar is equal to 1.0.

If no artificial dissipation is added, the damping characteristics of the numerical scheme are poor, in particular for θ_x approaching π (Fig. 6, top). This is due to the central discretization of the pressure terms (Eq. (25)) in the low-Mach AUSM scheme, resulting in poor pressure–velocity coupling. The scheme is stable because of the fourth order Runge–Kutta stepping.

Artificial dissipation, as described by Eq. (26), was gradually added by modifying the artificial dissipation parameter δ_{ad}. Addition of a small amount of artificial dissipation already results in improved damping, especially for θ_x approaching π. The optimal value for δ_{ad} was found to be 0.5. A higher value of δ_{ad} does not result in further improvement of the damping.

The 3D test case riser simulation shows very poor convergence behaviour if no artificial dissipation is added to the scheme (not shown). Furthermore, wiggles are observed in the calculated flow field.

Provided that artificial dissipation is added, the low-Mach AUSM scheme behaves well and wiggles are dissipated.

6.1.3. The grid aspect ratio: point versus plane solver

Fig. 7 compares the stability characteristics of the semi-implicit point solver and the semi-implicit plane solver for grid aspect ratios gar equal to 2.0 and 10.0.

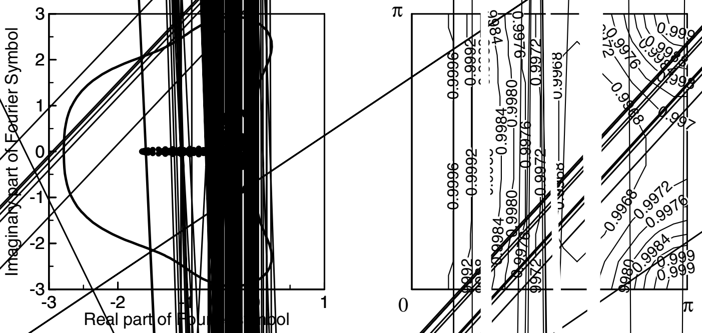

No artificial dissipation

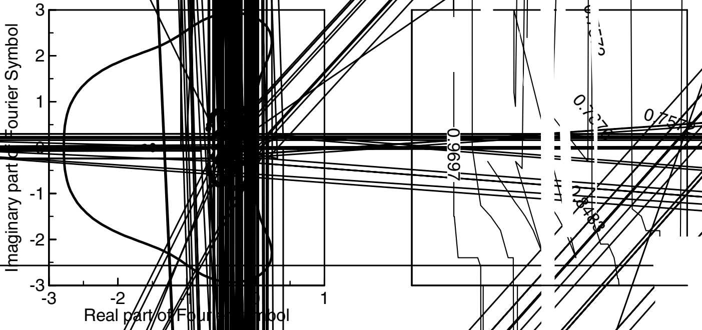

Artificial dissipation with $\delta_{ad} = 0.1$

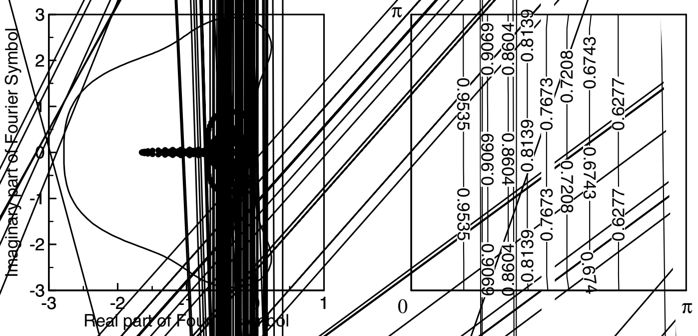

Artificial dissipation with $\delta_{ad} = 0.5$

Fig. 6. Influence of artificial dissipation. Stability results for turbulent viscous flow aligned with the x direction. Conditions: $\varepsilon_s = 5 \times 10^{-2}$, gar = 10.0, $k = 6.0$, $\varepsilon = 20.0$, $\Theta = 3.5$, [illegible] 1%, CFL = 1.0. Integration algorithm: plane solver, preconditioning, implicit treatment of source terms. Left: Fourier symbols in the complex plane; right: amplification factor.

For a grid aspect ratio gar of 1.0, the convergence behaviour of the point and plane solver is very similar (not shown). For higher grid aspect ratios, the pseudo-time step is reduced when using the point solver because of the stability restriction due to the acoustic terms in the y direction (Eq. (7)). For a grid aspect ratio of 2.0 (Fig. 7, top half), damping is slowing down with the point solver. For a grid aspect ratio of

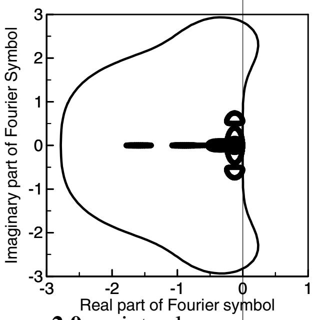

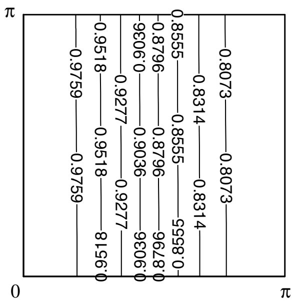

***gar* = 2.0:** point solver

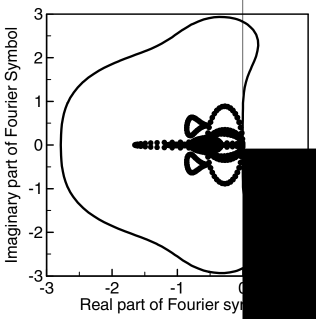

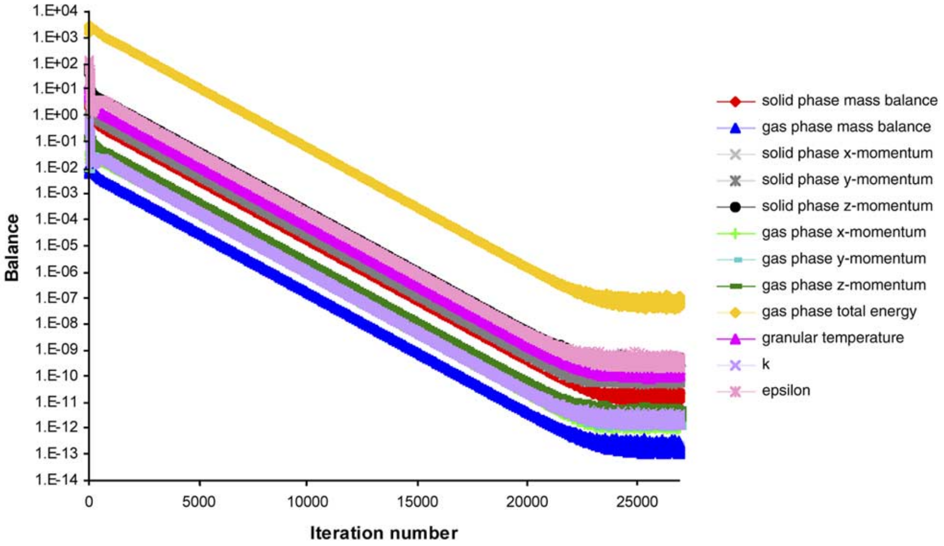

point solver

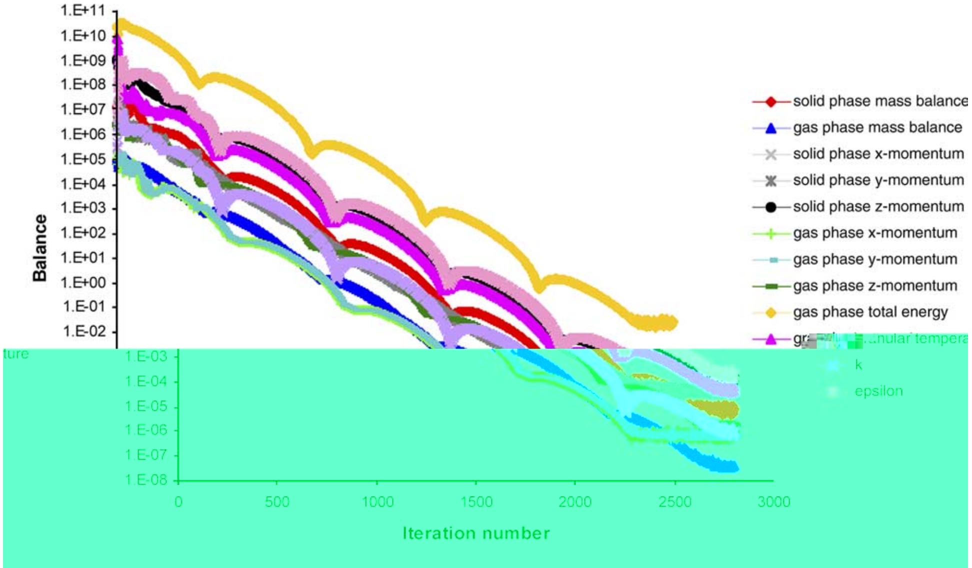

plane solver

Fig. 8. Point versus plane solver at high grid aspect ratios. Convergence plots for 3D test case riser simulations (Table 2, left; Fig. 2, left): gar = 10.0: CFL = 2.0. Integration algorithm: artificial dissipation $\delta_{\mathrm{ad}} = 0.5$, implicit treatment of source terms.

10.0 (Fig. 7, bottom half) or higher, the amplification factor is around unity in the whole (θ_x, θ_y) plane. If the plane solver is used with planes in the direction of the smallest grid size (y direction), the influence of the grid aspect ratio disappears completely. With the plane solver, convergence for higher grid aspect ratios is comparable to the case with a grid aspect ratio equal to unity.

The results from the Fourier analysis are confirmed by the 3D test case riser simulations, with a grid aspect ratio of about 10. Fig. 8 shows the convergence plots for both the point and the plane solver with

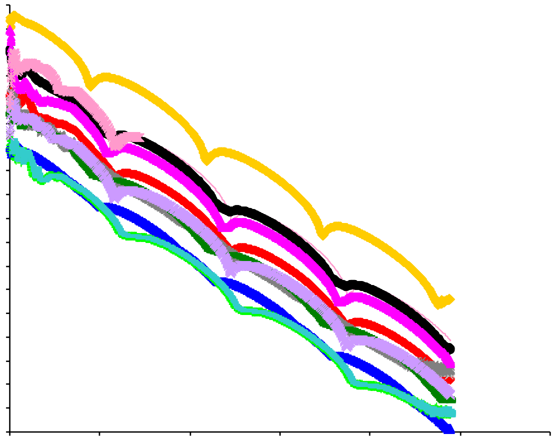

a CFL number of 2.0. Both the point and the plane solver converge exponentially, but the point solver converges much slower than the plane solver. Remark by comparing the convergence plots of the preconditioned plane solver in Fig. 4 (bottom), using a CFL number of 1.0, and Fig. 8 (bottom), using a CFL number of 2.0, that an increase of the CFL number indeed quasi proportionally increases the convergence speed. With a CFL number of 1.0, about 5800 iterations are required to reach convergence, whereas with a CFL number of 2.0 only 2800 iterations are required. Theoretically, the fourth-order Runge–Kutta stepping is stable up to $\mathrm{CFL} = 2\sqrt{2} = 2.8$.

Figs. 8 and 9 further investigate the grid aspect ratio independency of the convergence behaviour for the plane solver. With a grid aspect ratio of 10.0 (Fig. 8), convergence is seen to be equally fast as with a grid aspect ratio of 1.0 (Fig. 9), as predicted by the Fourier analysis.

It should be noted that an explicit approach was found to be unstable (not shown). Furthermore, a semi-implicit (point or plane wise) approach is required for as well the convective, the acoustic as the viscous terms to obtain a stable simultaneous solution algorithm (not shown). This is in contrast with single phase flows for which a semi-implicit approach of the convective terms was found not to be essential [32].

6.1.4. The viscous terms

The influence of viscous terms on the stability of the integration algorithm is investigated in Fig. 10. First, inviscid flow is investigated (Fig. 10, top), i.e., all viscous terms in the equations are neglected. The grid aspect ratio gar is equal to 1.0.

Compared with the viscous flow case (Fig. 3, bottom), the damping obtained for the inviscid flow case is equal. The integration techniques applied for the convective and acoustic terms, i.e., the semi-implicit approach in combination with the use of artificial dissipation and preconditioning, minimize the stabilizing effect from the viscous terms.

Next, the stability of the integration algorithm in a viscous stagnation zone is investigated by considering a zero value for the convective velocities (Fig. 10, middle). Remarkably, even for a small solids volume fraction, the numerical scheme is unstable. This could be due to the fact that stagnant gas–solid flow in a gravitational field is unphysical. To investigate this further, the stability analysis of the viscous stagnation zone

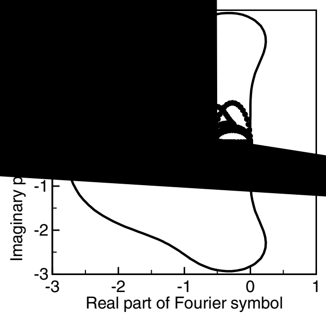

is also performed in a gravitationless field (Fig. 10, bottom). In this case, the numerical scheme is seen to be stable. Good damping is predicted, although for π-waves the damping remains less good.

6.1.5. *The treatment of the source terms*

In Fig. 11, the influence of the treatment of the drag source terms on the numerical stability of the simultaneous solution algorithms is investigated. The results are analogous for the gravity source terms. Viscous turbulent flow aligned with the *x* direction is investigated with a grid aspect ratio gar equal to 1.0.

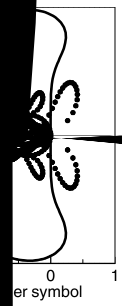
0
1
er symbol

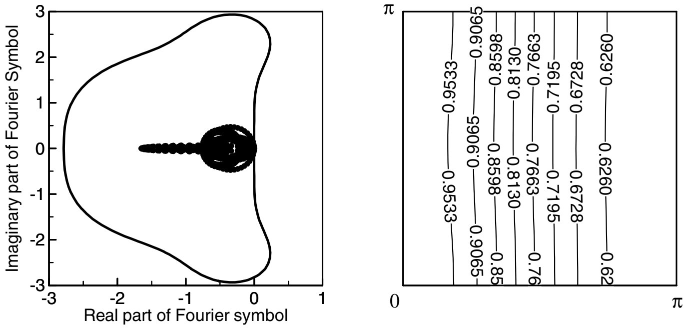

$\varepsilon_s = 5*10^{-6}$

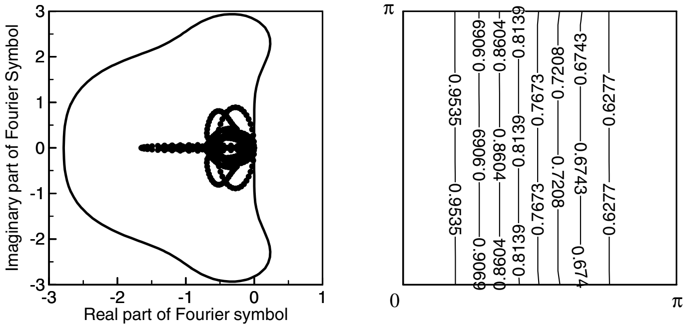

$\varepsilon_s = 5*10^{-2}$

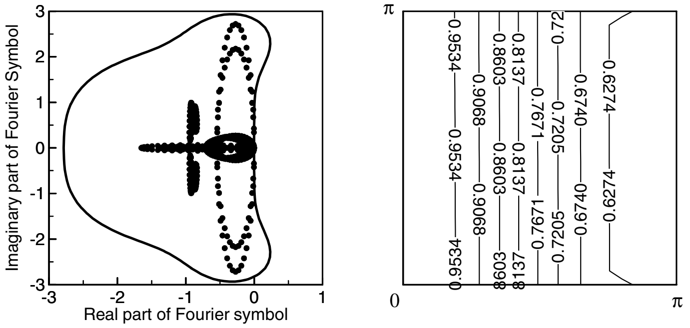

$\varepsilon_s = 4*10^{-1}$

Fig. 12. Influence of the solids volume fraction. Stability results for turbulent viscous flow aligned with the x direction. Conditions: gar = 10.0, $k = 6.0$, $\varepsilon = 20.0$, $\Theta = 3.5$, slip = 1%, CFL = 1.0. Integration algorithm: plane solver, artificial dissipation $\delta_{\mathrm{ad}} = 0.5$, preconditioning, implicit treatment of source terms. Left: Fourier symbols in the complex plane; right: amplification factor.

First, the stability of the simultaneous solution algorithms is investigated in the absence of drag source terms (Fig. 11, top). The simultaneous solution algorithms are seen to be unstable in this case, showing some regions with damping factors larger than unity. A possible reason for this, is that in the absence of a drag term, the gas–solid flow model that is used (Table 1) is unphysical by absence of a driving force for the solid phase.

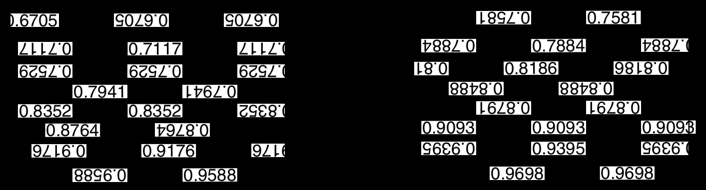
0.6705
0.6705
0.6705
0.7117
0.7117
0.7117
0.7529
0.7529
0.7529
0.7941
0.7941
0.8352
0.8352
0.8352
0.8764
0.8764
0.9176
0.9176
0.9176
0.9588
0.9588
0.7581
0.7581
0.7884
0.7884
0.7884
0.81
0.8186
0.8186
0.8488
0.8488
0.8791
0.8791
0.9093
0.9093
0.9093
0.9395
0.9395
0.9395
0.9698
0.9698

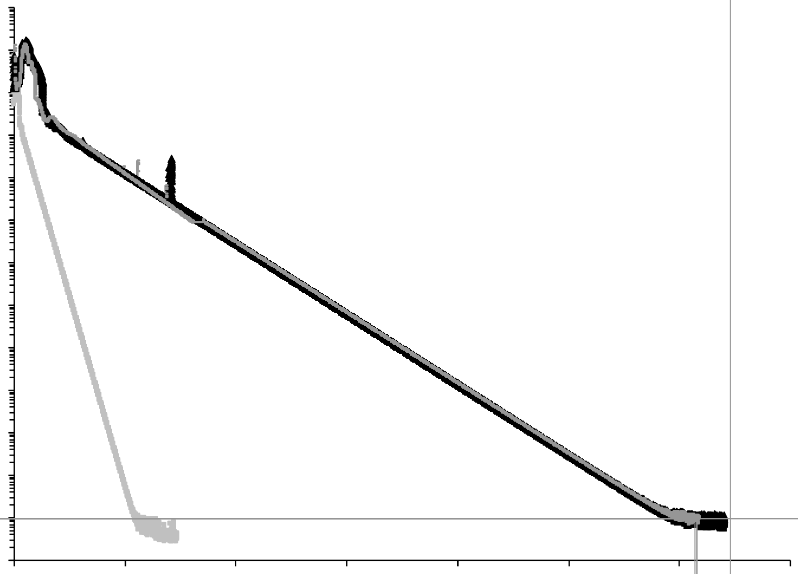

convergence is slow. This was indeed observed in previous work [4]. To obtain good damping, a fully implicit treatment of the drag and gravity source terms is necessary (Fig. 11, bottom). The 3D test case riser simulations confirm that convergence with a fully implicit treatment of these source terms is satisfying (Fig. 4, bottom and Figs. 8 and 9).

As mentioned before, the possibility of a fully implicit treatment of the source terms is a particular advantage of the simultaneous solution algorithms for multi-phase flows.

6.2. *Influence of the simulation conditions*

In the next paragraphs, the influence of the solids volume fraction and the gas–solid slip velocity, two important conditions in the simulation of gas–solid flows, is investigated for the simultaneous solution algorithms found optimal, i.e., applying preconditioning, artificial dissipation and a fully implicit treatment of the source terms.

6.2.1. The solids volume fraction

Fig. 12 illustrates the numerical stability of the simultaneous solution algorithms for varying solids volume fraction. The grid aspect ratio gar is equal to 1.0.

Provided that the preconditioner (Eqs. (14)–(19)) is scaled properly for the model that is used, i.e., according to the mixture speed of sound hold by the model, not much effect of the solids volume fraction on the amplification factors (Fig. 12, right) of the simultaneous solution algorithms is observed. Both for low and high solids volume fractions, the simultaneous solution algorithms provide good damping. However, from the Fourier symbol (Fig. 12, left) it is seen that with increasing solids volume fraction, the border of the stability region of the fourth-order Runge–Kutta scheme is approached. This could indicate that a further improvement of the preconditioner can still be achieved.

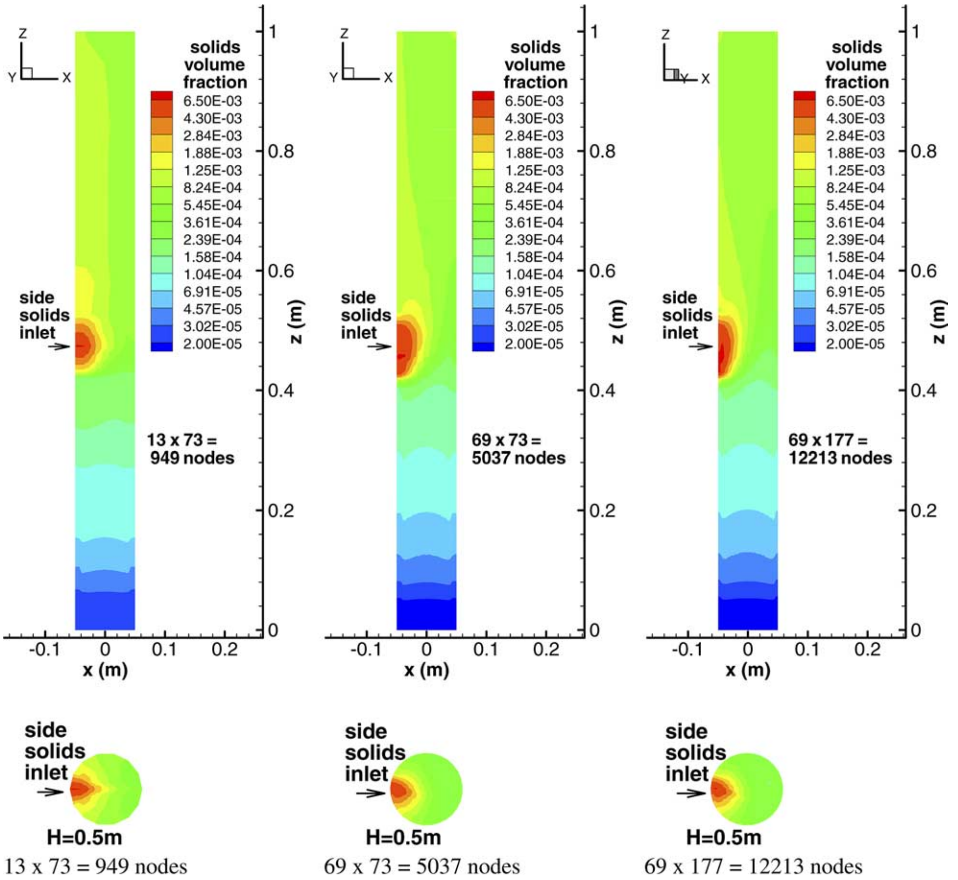

13 x 73 = 949 nodes 69 x 73 = 5037 nodes 69 x 177 = 12213 nodes

Fig. 15. Grid independency study. 3D validation case riser simulations (Table 2, right; Fig. 2, right): CFL = 1.0. Solids volume fraction profiles in an axial cross section through the side solids inlet and in a horizontal cross section at height of the side solids inlet (0.5 m height in the riser). Integration algorithm: plane solver, artificial dissipation $\delta_{ad} = 0.5$, implicit treatment of source terms. Cases shown: reference case: 13 planes of 73 nodes; axial mesh refinement: 69 planes of 73 nodes; mesh refinement both axial and in the plane: 69 planes of 177 nodes.

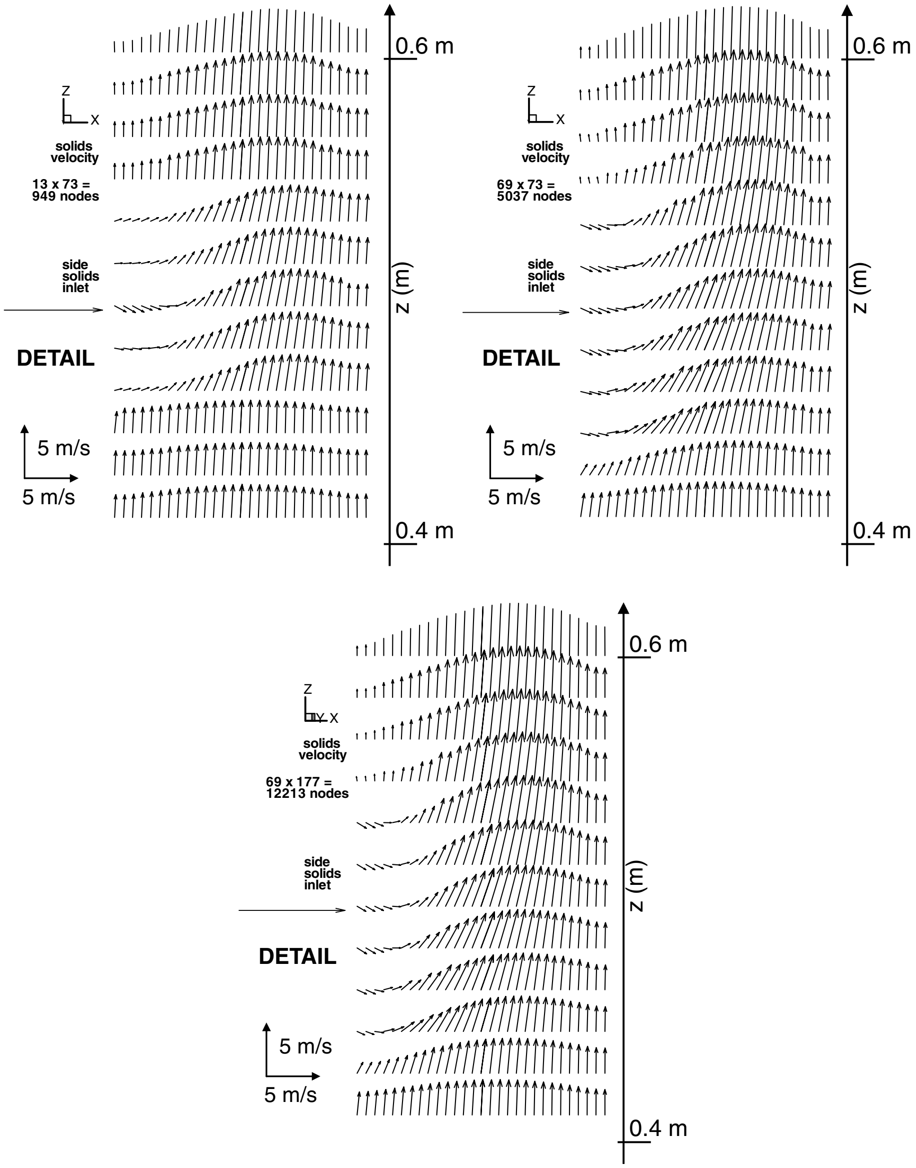

Fig. 16. Grid independency study. 3D validation case riser simulations (Table 2, right; Fig. 2, right): CFL = 1.0. Solids velocity vector plots in a detail of the cross section through the side solids inlet (interpolated). Integration algorithm: plane solver, artificial dissipation $\delta_{ad} = 0.5$, implicit treatment of source terms. Cases shown: reference case: 13 planes of 73 nodes; axial mesh refinement: 69 planes of 73 nodes; mesh refinement both axial and in the plane: 69 planes of 177 nodes.

6.2.2. The slip velocity

Fig. 13 investigates the effect of the value of the gas–solid slip velocity on the numerical stability of the simultaneous solution algorithms. The grid aspect ratio gar is equal to 1.0.

With increasing gas–solid slip, the simultaneous solution algorithms remain stable and the damping is seen to get only slightly affected. In the 3D test case riser simulations, no markable effect on the convergence of increased gas–solid slip in the bottom acceleration zone of the riser was observed.

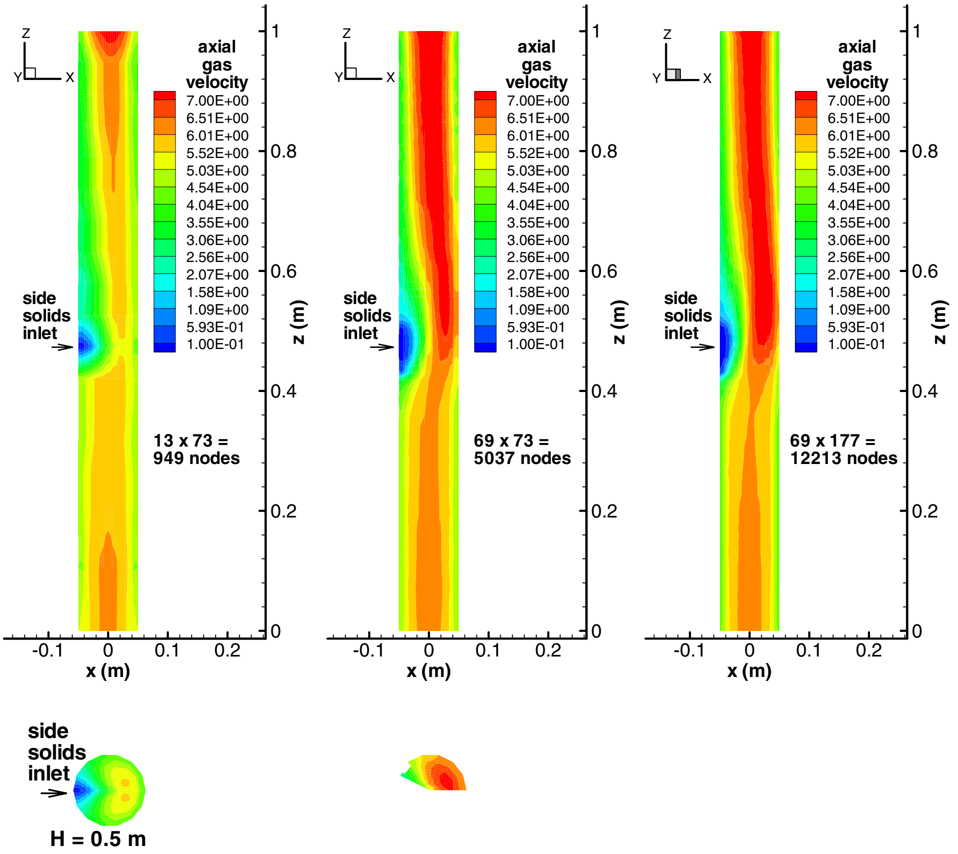

7. Experimental validation and grid independency study

The gas–solid flow model (see paragraph on gas–solid flow model and Table 1) and the solution algorithm presented (see paragraph on Integration scheme) are validated using experimental data of the bottom section of a cold-flow riser with a side solids inlet configuration. The latter induces a complex flow pattern with strong gradients in the flow field variables, e.g. the solids volume fraction or the velocities. Hence, the bottom acceleration zone of the riser in the vicinity of the side solids inlet is particularly suited for the validation of gas–solid flow models and solution algorithms.

In combination with the experimental validation, a grid independency study of the simulation results is carried out. Of particular interest with respect to the solution algorithm presented, the grid independency study allows to investigate the effect of mesh refinement in the different directions on the convergence behaviour and the memory and calculation time requirements.

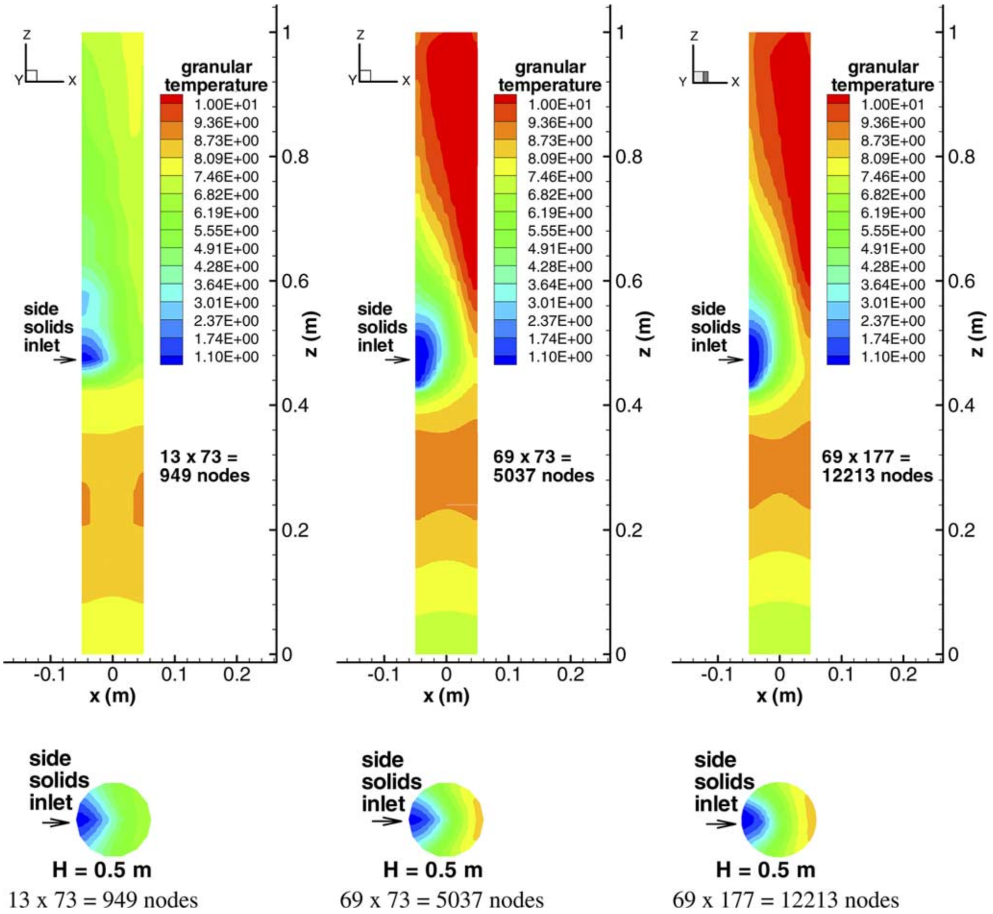

Fig. 18. Grid independency study. 3D validation case riser simulations (Table 2, right; Fig. 2, right): CFL = 1.0. Granular temperature profiles in an axial cross section through the side solids inlet and in a horizontal cross section at height of the side solids inlet (0.5 m height in the riser). Integration algorithm: plane solver, artificial dissipation $\delta_{ad} = 0.5$, implicit treatment of source terms. Cases shown: reference case: 13 planes of 73 nodes; axial mesh refinement: 69 planes of 73 nodes; mesh refinement both axial and in the plane: 69 planes of 177 nodes.

7.1. Side solids inlet flow case

Fig. 2 (right) shows a schematic representation of the bottom section of the experimental cold-flow pilot scale riser. The riser has a diameter of 0.1 m. The side solids inlet has a diameter of 0.08 m and is positioned at about 0.5 m height in the riser, making a 35° angle with the vertical z-axis. A 3D laser Doppler anemometer (LDA) is used to measure the local mean and fluctuating particle velocities under dilute phase conditions. Details on the complete experimental set-up can be found in [31].

The experimental and simulation conditions are shown in Table 2 (right). The axial gas inlet velocity was $5.31\ \mathrm{m\,s^{-1}}$. The solids have a mean particle diameter of 77 μm and a density of $1550\ \mathrm{kg\,m^{-3}}$. The solids flux is mechanically controlled by means of a diaphragm valve. The solids flux in the riser was $3\ \mathrm{kg\,m^{-2}\,s^{-1}}$.

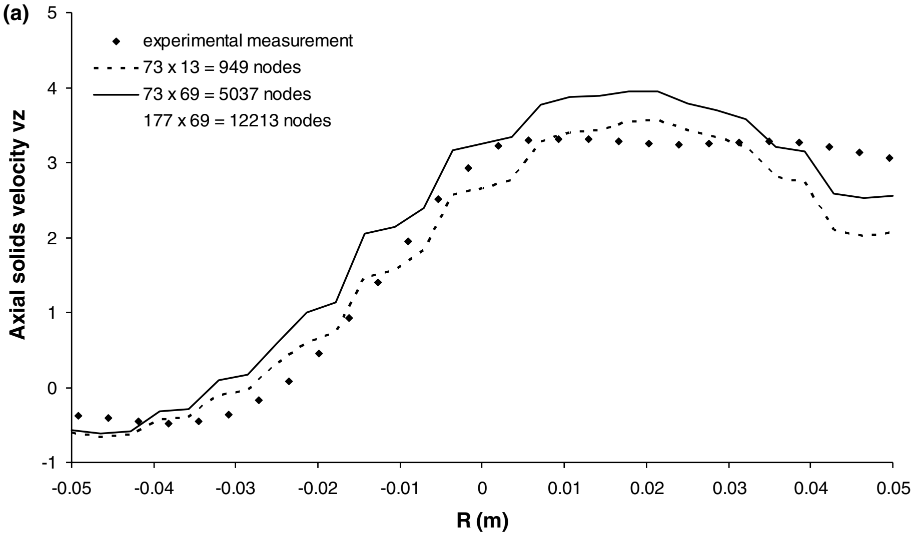

H = 0.5 m (= side solids inlet height)

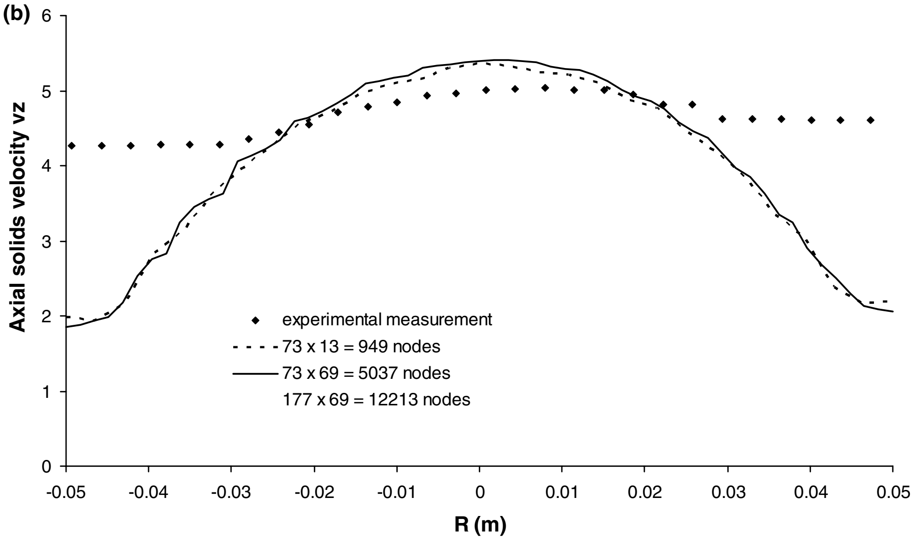

H = 1.0 m (= 0.5 m downstream of side solids inlet)

Fig. 19. Grid independency study: quantitative comparison with experimental results. 3D validation case riser simulations (Table 2, right; Fig. 2, right): CFL = 1.0. Axial solids velocity in a cross section through the side solids inlet: (a) at height of the side solids inlet (0.5 m height in the riser); (b) 0.5 m downstream of the side solids inlet (1.0 m height in the riser). Experimental data of Van engelandt et al. [31]. Integration algorithm: plane solver, artificial dissipation $\delta_{ad} = 0.5$, implicit treatment of source terms. Cases shown: reference case: 13 planes of 73 nodes; axial mesh refinement: 69 planes of 73 nodes; mesh refinement both axial and in the plane: 69 planes of 177 nodes.

The simulations are limited to the riser part of the set-up, i.e., the flow in the side solids inlet channel is not calculated. The computational mesh used for the riser simulations approaches the side solids inlet boundary as a rectangle of equal inlet surface area as the experimental side solids inlet. The value of the solids velocity components at the side solids inlet boundary required for the simulations (Table 2,

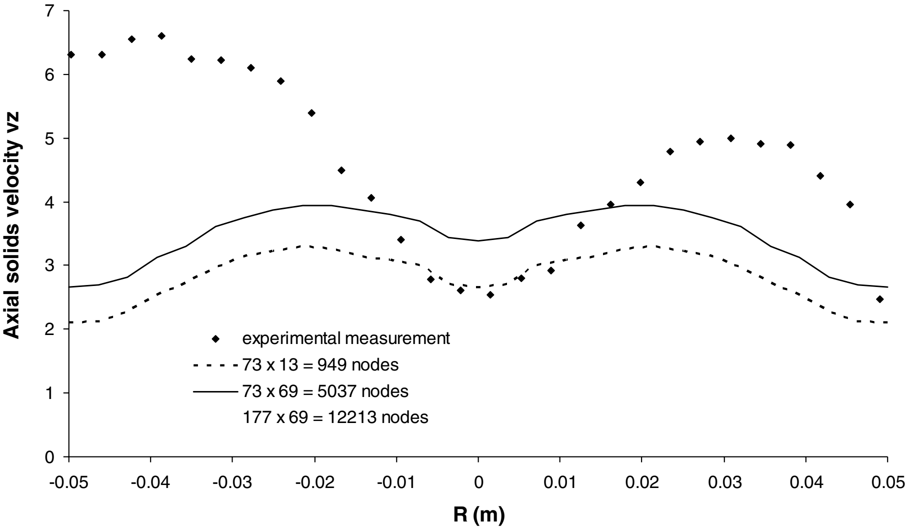

H = 0.5 m (= side solids inlet height)

Fig. 20. Grid independency study: quantitative comparison with experimental results. 3D validation case riser simulations (Table 2, right; Fig. 2, right): CFL = 1.0. Axial solids velocity in a cross section facing the side solids inlet at height of the side solids inlet (0.5 m height in the riser). Experimental data of Van engelandt et al. [31]. Integration algorithm: plane solver, artificial dissipation $\delta_{ad} = 0.5$, implicit treatment of source terms. Cases shown: reference case: 13 planes of 73 nodes; axial mesh refinement: 69 planes of 73 nodes; mesh refinement both axial and in the plane: 69 planes of 177 nodes.

right), were measured experimentally. A problem, however, arises with the value of the solids volume fraction to be imposed at the side solids inlet boundary. Visual observations and estimates of the solids volume fraction obtained from the experimental data rate show a non-uniform distribution of the solids over the side solids inlet boundary cross section. As a result of the gravitational force, solids accumulate in the lower section of the side solids inlet channel. In general, less than one third of the side solids inlet cross sectional surface area is used by the solids. In some cases, the solids are observed to enter the riser as a dense solids jet, using only a fraction of the side solids inlet cross sectional surface area. To account for solids accumulation at the side solids inlet boundary in the simulations while keeping the solids flux in the riser at its set-value, the side solids inlet height was reduced to about one third of its design value and the solids fraction at the side solids inlet boundary was increased by a factor three to 0.0056 (Table 2, right). Hence, although the experimental set-up is described as closely as possible, a certain incertainty exists due to the lack of data on the solids distribution at the boundary of the side solids inlet with the riser.

7.2. Effect of grid refinement on the convergence behaviour of the solution algorithm

Fig. 14 shows the convergence behaviour obtained with the horizontal plane solver using three different grid resolutions. The residual on the solids mass balance is shown but the behaviour for the other equations is similar (see, e.g., Figs. 4, 8 and 9).

With the reference coarse grid, 13 horizontal planes are distributed along the vertical axis of the riser and 73 nodes are distributed in each horizontal plane. Using a CFL-number of 1.0, about 5500 iterations are required to reach convergence. The residual on the balances have dropped by 11 orders of magnitude for all equations.

Refining the grid in the axial direction, i.e., increasing the number of horizontal planes distributed along the vertical axis of the riser from 13 to 69, about 29000 iterations are required to reach convergence (Fig. 14). As expected with a plane solver, the number of iterations required for convergence increases linearly with the number of planes.

Further refinement of the grid in the plane-wise directions, increasing the number of nodes per horizontal plane from 73 to 177, does not alter the number of iterations required for convergence (Fig. 14). As expected with a plane solver, the number of iterations required for convergence is independent of the number of nodes per horizontal plane. On the other hand, because the calculation time per horizontal plane increases with the number of nodes in the horizontal plane, the calculation time per iteration and the overall calculation time increase as a result of grid refinement in the plane-wise directions. Table 3 shows the calculation time and memory requirements for the three grids used. As expected for the plane solver, the calculation time per iteration increases linearly with the number of planes. Because the number of iterations required for convergence increases also linearly with the number of planes, the overall calculation time increases with the square of the number of planes. The calculation time per iteration increases more than proportional with the number of nodes in the plane-wise directions, but less than proportional with the square of the number of nodes in the plane-wise directions. The calculation time of the sparse direct solver used for the calculation of each horizontal plane (Eq. (39)) is proportional with the square of the bandwidth of the equation set Eq. (39). Intelligent mapping of the nodes in the plane-wise directions can reduce the bandwidth of the equation set Eq. (39) significantly.

The memory requirement increases somewhat less than proportional with the number of grid nodes, independent of the direction of the grid refinement. This is in accordance with the expectations.

7.3. *Effect of the grid resolution on the simulation results*

Figs. 15–18 show respectively the calculated profiles of the solids volume fraction, the solids velocity vector, the axial gas phase velocity and the granular temperature in an axial cross section of the riser through the side solids inlet and, for the contour plots, in a horizontal cross section at height of the side solids inlet (0.5 m height in the riser). Fig. 17 focuses on the immediate vicinity of the side solids inlet.

As seen from Fig. 15, the solids are quickly radially distributed over the entire cross section of the riser. Fig. 17 shows that the gas phase bypasses the dense zone near the side solids inlet, mainly via the side opposite the side solids inlet, resulting in downflow of solids just below the side solids inlet boundary (Fig. 16). Bypassing also occurs aside of the side solids inlet (see further Fig. 20), in the direction perpendicular to the axial cross section shown in Figs. 15–18.

Fig. 18 shows that the granular temperature in the vicinity of the side solids inlet is low and increases as the solid particles are entrained. This is qualitatively in agreement with the experimental observations of [31].

With respect to grid independency of the simulation results, Figs. 15–18 show that increasing the number of horizontal planes from 13 to 69 and, hence, the number of grid nodes from 949 to 5074, quantitatively alters the calculated flow field. Further increasing the number of grid nodes from 5074 to 12213 by increasing the number of nodes per plane from 73 to 177, hardly alters the calculated flow field (Figs. 15–18). Hence, the grid is sufficiently refined for the simulation results to become grid independent. In such case, the simulation results are only determined by the gas–solid flow model (see paragraph on gas–solid flow model), not by numerical issues. The latter is important with respect to the experimental validation, discussed in the next paragraph.

7.4. Experimental validation

Figs. 19 and 20 compare simulated and experimentally measured axial solids velocities. Fig. 19 shows the axial solids velocities in an axial cross section through the side solids inlet (positioned at the left in Fig. 19(a)) at height of the side solids inlet (0.5 m height in the riser) (Fig. 19(a)) and 0.5 m downstream of the side solids inlet (1.0 m height in the riser) (Fig. 19(b)). At height of the side solids inlet (Fig. 19(a)), the experimental and simulated values correspond well. In this section of the riser, the influence of the solid wall on the flow field is limited and the gas–solid flow model (see paragraph on gas–solid flow model and Table 1) is seen to perform well. At 1.0 m height in the riser, 0.5 m downstream of the side solids inlet, both the experimental observations and the simulations show that the inlet effects have completely dissipated. In the core of the riser, the experimental and simulated values correspond reasonably well. Near the solid wall, on the other hand, the gas–solid flow model underestimates the axial solids velocities. Qualitatively, both the experimental observations and the simulations show that the axial solids velocity profile flattens out when approaching the solid wall.

Remark that, as demonstrated by the grid independency study in the previous paragraph, the deviation between the experimental and simulated values is not related to the simultaneous solution algorithm investigated but is related to the gas–solid flow model (see paragraph on gas–solid flow model). A possible origin of the deviation between the experimental and simulated values near the solid wall is found in the solid wall boundary conditions that are used, both for the gas and the solid phase (see paragraph on gas–solid flow model). The standard wall functions used for the gas phase need to be modified to account for gas–solid interactions and probably overestimate the wall shear stress. For the solid phase, the boundary conditions derived by Sinclair and Jackson [29] and adopted in this work do not account for solid particles rolling along the solid wall and, hence, also probably overestimate the wall shear stress.

Fig. 20 compares the experimentally measured and simulated axial solids velocity profile in an axial cross section of the riser facing the side solids inlet at height of the side solids inlet (0.5 m height in the riser) and confirms a possible role of the solid wall boundary conditions. Qualitatively, the simulations predict well bypassing aside of the side solids inlet, resulting in a decrease of the axial solids velocity in the center of the riser and off-center maxima in the axial solids velocity profile. In the core of the riser, the axial solids velocity is reasonably well predicted, taking into consideration the uncertainty on the values of the solids volume fraction at the side solids inlet boundary and the actual side solids inlet boundary surface area (see paragraph on Side solids inlet flow case). Near the solid wall, however, the axial solids velocity is again underestimated, although the deviation is more pronounced at the left than at the right of the side solids inlet. Remark that the asymmetry in the experimental observations in Fig. 20 is probably due to an asymmetry, i.e. a bend, in the gas feeding channel to the riser in the experimental set-up, not accounted for in the simulations.

Summarizing, the experimental validation and the grid independency study show that the simultaneous solution algorithm for the Eulerian–Eulerian gas–solid flow models presented in this paper performs well. The gas–solid flow model, on the other hand, in particular the solid wall boundary conditions, needs to be improved.

8. Conclusions

Fourier analysis of simultaneous solution algorithms for Eulerian–Eulerian gas–solid flow models shows that these integration algorithms can provide good damping independent of the solids volume fraction and the gas–solid slip velocity. Whereas the use of a semi-implicit point solver is restricted to low grid aspect ratios, the semi-implicit plane solver is seen to perform well, independently of the grid aspect ratio. Preconditioning is shown to be essential to obtain good damping. Proper scaling of the preconditioner, accounting for the model mixture speed of sound, is necessary to obtain damping independent of the solids volume fraction. The low-Mach AUSM scheme imposes the introduction of artificial dissipation to obtain good damping, due to the central pressure discretization. To guarantee numerical stability, a fully implicit treatment of the drag and gravity source terms is required. In this case, the stability of the integration scheme is not much affected by the presence of these source terms. The possibility of a fully implicit approach for the source terms is a particular advantage of the simultaneous solution algorithms.

Good agreement between the stability predictions from the 2D Fourier analysis and the convergence behaviour of 3D riser simulations is found.

A grid independency study is carried out. The grid was sufficiently refined for the solutions to become grid independent. For the plane solver, the number of iterations required for convergence increases linearly with the number of planes and is independent of the number of nodes per plane. The calculation time per iteration, on the other hand, increases linearly with the number of planes but increases more than proportional with the number of nodes per plane.

Experimental validation of simulations of the bottom zone of a riser with a side solids inlet shows that the Eulerian–Eulerian gas–solid flow models, in particular the solid wall boundary conditions, need to be further developed.

Acknowledgments

The "Instituut voor de aanmoediging van Innovatie door Wetenschap en Technologie in Vlaanderen (IWT-Vlaanderen)" is greatly acknowledged for the financial support under Contract IWT/OZM/020059.

The "Bijzonder Onderzoeksfonds van de Universiteit Gent" and the IAP programme of the DTWC office are greatly acknowledged for the financial support of the FCC-research.

One of the authors (J.D.W.) thank Dr. Meng-Sing Liou of the NASA Glenn Research Center for his explanations on the AUSM-scheme in the beginning of this work. One of the authors (JDW) would like to thank J. Nollet for the useful discussions.

Appendix A

Introducing:

$$Fg_x = \varepsilon_g \rho_g u_x, \tag{AI.1}$$

$$Fg_y = \varepsilon_g \rho_g u_y, \tag{AI.2}$$

$$Fs_x = \varepsilon_s \rho_{sp} v_x, \tag{AI.3}$$

$$Fs_y = \varepsilon_s \rho_{sp} v_y \tag{AI.4}$$

and making use of the discretization given by Eqs. (23) and (24), matrix A_c containing the terms in the x-direction for the convective fluxes can be written as:

$$
\begin{aligned}
A_{\mathrm{c}} = &\left[\begin{array}{ccccc}
\rho_{\mathrm{sp}} v_x \,\mathrm{d}x^{-1} & 0 & 0 & 0 & 0 \\
-\rho_{\mathrm{g}} u_x \,\mathrm{d}x^{-1} & Fg_x P^{-1} \,\mathrm{d}x^{-1} & 0 & 0 & 0 \\
\rho_{\mathrm{sp}} v_x v_x \,\mathrm{d}x^{-1} & 0 & Fs_x \,\mathrm{d}x^{-1} & 0 & 0 \\
\rho_{\mathrm{sp}} v_x v_y \,\mathrm{d}x^{-1} & 0 & 0 & Fs_x \,\mathrm{d}x^{-1} & 0 \\
-\rho_{\mathrm{g}} u_x u_x \,\mathrm{d}x^{-1} & Fg_x P^{-1} u_x \,\mathrm{d}x^{-1} & 0 & 0 & Fg_x \,\mathrm{d}x^{-1} \\
-\rho_{\mathrm{g}} u_x u_y \,\mathrm{d}x^{-1} & Fg_y P^{-1} u_x \,\mathrm{d}x^{-1} & 0 & 0 & 0 \\
-\rho_{\mathrm{g}} u_x E_{\mathrm{g}} \,\mathrm{d}x^{-1} & Fg_x P^{-1} E_{\mathrm{g}} \,\mathrm{d}x^{-1} & 0 & 0 & \varepsilon_{\mathrm{g}} \rho_{\mathrm{g}} u_x u_x \,\mathrm{d}x^{-1} \\
3 \cdot 2^{-1} \rho_{\mathrm{sp}} v_x \Theta \cdot \mathrm{d}x^{-1} & 0 & 0 & 0 & 0 \\
-\rho_{\mathrm{g}} u_x k \cdot \mathrm{d}x^{-1} & Fg_x P^{-1} k \cdot \mathrm{d}x^{-1} & 0 & 0 & 0 \\
-\rho_{\mathrm{g}} u_x \varepsilon \cdot \mathrm{d}x^{-1} & Fg_x P^{-1} \varepsilon \cdot \mathrm{d}x^{-1} & 0 & 0 & 0
\end{array}\right. \\
&\left.\begin{array}{ccccc}
0 & 0 & 0 & 0 & 0 \\
0 & -Fg_x T^{-1} \,\mathrm{d}x^{-1} & 0 & 0 & 0 \\
0 & 0 & 0 & 0 & 0 \\
0 & 0 & 0 & 0 & 0 \\
0 & -Fg_x T^{-1} u_x \,\mathrm{d}x^{-1} & 0 & 0 & 0 \\
Fg_x \,\mathrm{d}x^{-1} & -Fg_y T^{-1} u_x \,\mathrm{d}x^{-1} & 0 & 0 & 0 \\
Fg_x u_y \,\mathrm{d}x^{-1} & Fg_x \cdot \mathrm{d}x^{-1} \cdot \left(C_{V_{\mathrm{kg}}} - E_{\mathrm{g}} T^{-1} \right) & 0 & Fg_x \,\mathrm{d}x^{-1} & 0 \\
0 & 0 & 3 \cdot 2^{-1} Fs_x \,\mathrm{d}x^{-1} & 0 & 0 \\
0 & -Fg_x T^{-1} k \cdot \mathrm{d}x^{-1} & 0 & Fg_x \,\mathrm{d}x^{-1} & 0 \\
0 & -Fg_x T^{-1} \varepsilon \cdot \mathrm{d}x^{-1} & 0 & 0 & Fg_x \,\mathrm{d}x^{-1}
\end{array}\right].
\end{aligned}
\tag{AI.5}
$$

The matrix B_{c} containing the corresponding terms in the y-direction is derived analogously.

Due to the central discretization (Eq. (25)), the matrices A_{a} and B_{a} for the acoustic fluxes are given by

$$A_{\mathrm{a}} = [O], \tag{AI.6}$$

$$B_{\mathrm{a}} = [O]. \tag{AI.7}$$

Artificial dissipation according to Eq. (26) is added to all the gas phase equations, resulting in the following formulation for A_d containing the terms in the x-direction:

$$A_\mathrm{d} = \begin{bmatrix} 0 & 0 & 0 & 0 & 0 & 0 & 0 & 0 & 0 & 0 \\ 0 & (\delta_\mathrm{ad}/\beta_x)\cdot \mathrm{d}x^{-1} & 0 & 0 & 0 & 0 & 0 & 0 & 0 & 0 \\ 0 & 0 & 0 & 0 & 0 & 0 & 0 & 0 & 0 & 0 \\ 0 & 0 & 0 & 0 & 0 & 0 & 0 & 0 & 0 & 0 \\ 0 & (\delta_\mathrm{ad}/\beta_x)\cdot \mathrm{d}x^{-1}\cdot u_x & 0 & 0 & 0 & 0 & 0 & 0 & 0 & 0 \\ 0 & (\delta_\mathrm{ad}/\beta_x)\cdot \mathrm{d}x^{-1}\cdot u_y & 0 & 0 & 0 & 0 & 0 & 0 & 0 & 0 \\ 0 & (\delta_\mathrm{ad}/\beta_x)\cdot \mathrm{d}x^{-1}\cdot H_\mathrm{g} & 0 & 0 & 0 & 0 & 0 & 0 & 0 & 0 \\ 0 & 0 & 0 & 0 & 0 & 0 & 0 & 0 & 0 & 0 \\ 0 & (\delta_\mathrm{ad}/\beta_x)\cdot \mathrm{d}x^{-1}\cdot k & 0 & 0 & 0 & 0 & 0 & 0 & 0 & 0 \\ 0 & (\delta_\mathrm{ad}/\beta_x)\cdot \mathrm{d}x^{-1}\cdot \varepsilon & 0 & 0 & 0 & 0 & 0 & 0 & 0 & 0 \end{bmatrix}. \tag{AI.8}$$

The matrix B_d containing the corresponding terms in the y-direction is derived analogously. Discretization of the viscous fluxes following a central scheme results in:

$$A_\mathrm{v} = \left[\begin{matrix} 0 & 0 & 0 & 0 & 0 \\ 0 & 0 & 0 & 0 & 0 \\ 0 & 0 & \left[\varepsilon_\mathrm{s}\cdot\left(\xi_\mathrm{s} - 2\mu_\mathrm{s}3^{-1}\right) + 2\varepsilon_\mathrm{s}\mu_\mathrm{s}\right]\cdot \mathrm{d}x^{-2} & 0 & 0 \\ 0 & 0 & 0 & \varepsilon_\mathrm{s}\mu_\mathrm{s}\,\mathrm{d}x^{-2} & 0 \\ 0 & 0 & 0 & 0 & \left[\varepsilon_\mathrm{g}\cdot\left(\xi_\mathrm{g} - 2\mu_\mathrm{g}^\mathrm{tot}3^{-1}\right) + 2\varepsilon_\mathrm{g}\mu_\mathrm{g}^\mathrm{tot}\right]\cdot \mathrm{d}x^{-2} \\ 0 & 0 & 0 & 0 & 0 \\ 0 & 0 & 0 & 0 & \left[\varepsilon_\mathrm{g}\cdot\left(\xi_\mathrm{g} - 2\mu_\mathrm{g}^\mathrm{tot}3^{-1}\right) + 2\varepsilon_\mathrm{g}\mu_\mathrm{g}^\mathrm{tot}\right]\cdot u_x\cdot \mathrm{d}x^{-2} \\ 0 & 0 & 0 & 0 & 0 \\ 0 & 0 & 0 & 0 & 0 \\ 0 & 0 & 0 & 0 & 0 \end{matrix}\right.$$

$$\left.\begin{matrix} 0 & 0 & 0 & 0 & 0 \\ 0 & 0 & 0 & 0 & 0 \\ 0 & 0 & 0 & 0 & 0 \\ 0 & 0 & 0 & 0 & 0 \\ 0 & 0 & 0 & 0 & 0 \\ \varepsilon_\mathrm{g}\mu_\mathrm{g}^\mathrm{tot}\,\mathrm{d}x^{-2} & 0 & 0 & 0 & 0 \\ \varepsilon_\mathrm{g}\mu_\mathrm{g}^\mathrm{tot}\cdot u_y\cdot \mathrm{d}x^{-2} & \varepsilon_\mathrm{g}\lambda_\mathrm{g}^\mathrm{tot}\,\mathrm{d}x^{-2} & 0 & 0 & 0 \\ 0 & 0 & \varepsilon_\mathrm{s}\kappa\,\mathrm{d}x^{-2} & 0 & 0 \\ 0 & 0 & 0 & \varepsilon_\mathrm{g}\mu_\mathrm{g}^\mathrm{tot}\sigma_k^{-1}\,\mathrm{d}x^{-2} & 0 \\ 0 & 0 & 0 & 0 & \varepsilon_\mathrm{g}\mu_\mathrm{g}^\mathrm{tot}\sigma_\varepsilon^{-1}\,\mathrm{d}x^{-2} \end{matrix}\right]. \tag{AI.9}$$

The matrix B_v containing the corresponding terms in the y-direction is derived analogously.

An implicit treatment of the gravity source terms results in:

$$G_{\mathrm{L}}=\begin{pmatrix} 0 & 0 & 0 & 0 & 0 & 0 & 0 & 0 & 0 & 0\\ 0 & 0 & 0 & 0 & 0 & 0 & 0 & 0 & 0 & 0\\ \rho_{\mathrm{sp}}g_x & 0 & 0 & 0 & 0 & 0 & 0 & 0 & 0 & 0\\ \rho_{\mathrm{sp}}g_y & 0 & 0 & 0 & 0 & 0 & 0 & 0 & 0 & 0\\ -\rho_{\mathrm{sp}}g_x & 0 & 0 & 0 & 0 & 0 & 0 & 0 & 0 & 0\\ -\rho_{\mathrm{sp}}g_y & 0 & 0 & 0 & 0 & 0 & 0 & 0 & 0 & 0\\ -\rho_{\mathrm{sp}}\left(g_xu_x+g_yu_y\right) & 0 & 0 & 0 & -\varepsilon_{\mathrm{s}}\rho_{\mathrm{sp}}g_x & -\varepsilon_{\mathrm{s}}\rho_{\mathrm{sp}}g_y & 0 & 0 & 0 & 0\\ 0 & 0 & 0 & 0 & 0 & 0 & 0 & 0 & 0 & 0\\ 0 & 0 & 0 & 0 & 0 & 0 & 0 & 0 & 0 & 0\\ 0 & 0 & 0 & 0 & 0 & 0 & 0 & 0 & 0 & 0 \end{pmatrix}. \tag{AI.10}$$

In case only the negative part of the drag source term is treated implicitly, D_{L} is given by

$$D_{\mathrm{L}}=\begin{pmatrix} 0 & 0 & 0 & 0 & 0 & 0 & 0 & 0 & 0 & 0\\ 0 & 0 & 0 & 0 & 0 & 0 & 0 & 0 & 0 & 0\\ 0 & 0 & -\beta & 0 & 0 & 0 & 0 & 0 & 0 & 0\\ 0 & 0 & 0 & -\beta & 0 & 0 & 0 & 0 & 0 & 0\\ 0 & 0 & 0 & 0 & -\beta & 0 & 0 & 0 & 0 & 0\\ 0 & 0 & 0 & 0 & 0 & -\beta & 0 & 0 & 0 & 0\\ 0 & 0 & 0 & 0 & -\beta u_x & -\beta u_y & 0 & 0 & 0 & 0\\ 0 & 0 & 0 & 0 & 0 & 0 & 0 & 0 & 0 & 0\\ 0 & 0 & 0 & 0 & 0 & 0 & 0 & 0 & 0 & 0\\ 0 & 0 & 0 & 0 & 0 & 0 & 0 & 0 & 0 & 0 \end{pmatrix}. \tag{AI.11}$$

A fully implicit treatment results in

$$D_{\mathrm{L}}=\begin{pmatrix} 0 & 0 & 0 & 0 & 0 & 0 & 0 & 0 & 0 & 0\\ 0 & 0 & 0 & 0 & 0 & 0 & 0 & 0 & 0 & 0\\ 0 & 0 & -\beta & 0 & \beta & 0 & 0 & 0 & 0 & 0\\ 0 & 0 & 0 & -\beta & 0 & \beta & 0 & 0 & 0 & 0\\ 0 & 0 & \beta & 0 & -\beta & 0 & 0 & 0 & 0 & 0\\ 0 & 0 & 0 & \beta & 0 & -\beta & 0 & 0 & 0 & 0\\ 0 & 0 & \beta v_x & \beta v_y & -\beta u_x & -\beta u_y & 0 & 0 & 0 & 0\\ 0 & 0 & 0 & 0 & 0 & 0 & 0 & 0 & 0 & 0\\ 0 & 0 & 0 & 0 & 0 & 0 & 0 & 0 & 0 & 0\\ 0 & 0 & 0 & 0 & 0 & 0 & 0 & 0 & 0 & 0 \end{pmatrix}. \tag{AI.12}$$

Appendix B

Using functions *ce*() and *up*(), respectively, given by Eqs. (48) and (49), $\overset{\frown}{A}_{\mathrm{c}}(\theta)$ is derived as:

$$\overset{\frown}{A}_c(\theta) = \left[\begin{array}{ccc}
\rho_{\mathrm{sp}} v_x \cdot up(\theta, \mathrm{d}x) & 0 & \varepsilon_{\mathrm{s}} \rho_{\mathrm{sp}} \cdot ce(\theta, \mathrm{d}x) \\
-\rho_{\mathrm{g}} u_x \cdot up(\theta, \mathrm{d}x) & Fg_x P^{-1} \cdot up(\theta, \mathrm{d}x) & 0 \\
\rho_{\mathrm{sp}} v_x v_x \cdot up(\theta, \mathrm{d}x) & 0 & Fs_x \cdot (ce(\theta, \mathrm{d}x) + up(\theta, \mathrm{d}x)) \\
\rho_{\mathrm{sp}} v_x v_y \cdot up(\theta, \mathrm{d}x) & 0 & Fs_y \cdot ce(\theta, \mathrm{d}x) \\
-\rho_{\mathrm{g}} u_x u_x \cdot up(\theta, \mathrm{d}x) & Fg_x P^{-1} u_x \cdot up(\theta, \mathrm{d}x) & 0 \\
-\rho_{\mathrm{g}} u_x u_y \cdot up(\theta, \mathrm{d}x) & Fg_y P^{-1} u_x \cdot up(\theta, \mathrm{d}x) & 0 \\
-\rho_{\mathrm{g}} u_x E_{\mathrm{g}} \cdot up(\theta, \mathrm{d}x) & Fg_x P^{-1} E_{\mathrm{g}} \cdot up(\theta, \mathrm{d}x) & 0 \\
3 \cdot 2^{-1} \rho_{\mathrm{sp}} v_x \Theta \cdot up(\theta, \mathrm{d}x) & 0 & 3 \cdot 2^{-1} \varepsilon_{\mathrm{s}} \rho_{\mathrm{sp}} \Theta \cdot ce(\theta, \mathrm{d}x) \\
-\rho_{\mathrm{g}} u_x k \cdot up(\theta, \mathrm{d}x) & Fg_x P^{-1} k \cdot up(\theta, \mathrm{d}x) & 0 \\
-\rho_{\mathrm{g}} u_x \varepsilon \cdot up(\theta, \mathrm{d}x) & Fg_x P^{-1} \varepsilon \cdot up(\theta, \mathrm{d}x) & 0
\end{array}\right.$$

$$\begin{array}{ccc}
0 & 0 & 0 \\
0 & \varepsilon_{\mathrm{g}} \rho_{\mathrm{g}} \cdot ce(\theta, \mathrm{d}x) & 0 \\
0 & 0 & 0 \\
Fs_x \cdot up(\theta, \mathrm{d}x) & 0 & 0 \\
0 & Fg_x \cdot (ce(\theta, \mathrm{d}x) + up(\theta, \mathrm{d}x)) & 0 \\
0 & Fg_y \cdot ce(\theta, \mathrm{d}x) & Fg_x \cdot up(\theta, \mathrm{d}x) \\
0 & \varepsilon_{\mathrm{g}} \rho_{\mathrm{g}} \left(u_x u_x \cdot up(\theta, \mathrm{d}x) + E_{\mathrm{g}} \cdot ce(\theta, \mathrm{d}x)\right) & Fg_x u_y \cdot up(\theta, \mathrm{d}x) \\
0 & 0 & 0 \\
0 & \varepsilon_{\mathrm{g}} \rho_{\mathrm{g}} k \cdot ce(\theta, \mathrm{d}x) & 0 \\
0 & \varepsilon_{\mathrm{g}} \rho_{\mathrm{g}} \varepsilon \cdot ce(\theta, \mathrm{d}x) & 0
\end{array}$$

$$\left.\begin{array}{cccc}
0 & 0 & 0 & 0 \\
-Fg_x T^{-1} \cdot up(\theta, \mathrm{d}x) & 0 & 0 & 0 \\
0 & 0 & 0 & 0 \\
0 & 0 & 0 & 0 \\
-Fg_x T^{-1} u_x \cdot up(\theta, \mathrm{d}x) & 0 & 0 & 0 \\
-Fg_y T^{-1} u_x \cdot up(\theta, \mathrm{d}x) & 0 & 0 & 0 \\
Fg_x \cdot up(\theta, \mathrm{d}x) \cdot \left(C_{V_{\mathrm{kg}}} - E_{\mathrm{g}} T^{-1}\right) & 0 & Fg_x \cdot up(\theta, \mathrm{d}x) & 0 \\
0 & 3 \cdot 2^{-1} Fs_x \cdot up(\theta, \mathrm{d}x) & 0 & 0 \\
-Fg_x T^{-1} k \cdot up(\theta, \mathrm{d}x) & 0 & Fg_x \cdot up(\theta, \mathrm{d}x) & 0 \\
-Fg_x T^{-1} \varepsilon \cdot up(\theta, \mathrm{d}x) & 0 & 0 & Fg_x \cdot up(\theta, \mathrm{d}x)
\end{array}\right], \tag{AII.1}$$

where Fg_x, Fg_y, Fs_x, and Fs_y are given by Eqs. (AI.1)–(AI.4) (Appendix A). $\overset{\frown}{B}_c(\theta)$ is derived analogously.

For the acoustic part, the following matrix containing the terms in the x-direction is obtained:

$$\widehat{A}_a(\theta) = \left[\begin{matrix} 0 & 0 & 0 & 0 & 0 \\ 0 & 0 & 0 & 0 & 0 \\ \left(\rho_{\mathrm{sp}}\Theta + 2(2(1+e)g_{r\mathrm{df}})\varepsilon_{\mathrm{s}}\rho_{\mathrm{sp}}\Theta\right)\cdot ce(\theta,\,\mathrm{d}x) & 0 & 0 & 0 & 0 \\ 0 & 0 & 0 & 0 & 0 \\ 0 & \left(1 + 2\cdot 3^{-1}\rho_{\mathrm{g}}k\cdot P^{-1}\right)\cdot ce(\theta,\,\mathrm{d}x) & 0 & 0 & 0 \\ 0 & 0 & 0 & 0 & 0 \\ 0 & \left(1 + 2\cdot 3^{-1}\rho_{\mathrm{g}}k\cdot P^{-1}\right)u_x\cdot ce(\theta,\,\mathrm{d}x) & 0 & 0 & \left(P + 2\cdot 3^{-1}\rho_{\mathrm{g}}k\right)\cdot ce(\theta,\,\mathrm{d}x) \\ 0 & 0 & 0 & 0 & 0 \\ 0 & 0 & 0 & 0 & 0 \\ 0 & 0 & 0 & 0 & 0 \end{matrix}\right.$$

$$\left.\begin{matrix} 0 & 0 & 0 & 0 & 0 \\ 0 & 0 & 0 & 0 & 0 \\ 0 & 0 & \left((1+2(1+e)\varepsilon_{\mathrm{s}}g_{r\mathrm{df}})\varepsilon_{\mathrm{s}}\rho_{\mathrm{sp}}\right)\cdot ce(\theta,\,\mathrm{d}x) & 0 & 0 \\ 0 & 0 & 0 & 0 & 0 \\ 0 & -2\cdot 3^{-1}\rho_{\mathrm{g}}k\cdot T^{-1}\cdot ce(\theta,\,\mathrm{d}x) & 0 & 2\cdot 3^{-1}\rho_{\mathrm{g}}\cdot ce(\theta,\,\mathrm{d}x) & 0 \\ 0 & 0 & 0 & 0 & 0 \\ 0 & -2\cdot 3^{-1}\rho_{\mathrm{g}}k\cdot T^{-1}u_x\cdot ce(\theta,\,\mathrm{d}x) & 0 & 2\cdot 3^{-1}\rho_{\mathrm{g}}u_x\cdot ce(\theta,\,\mathrm{d}x) & 0 \\ 0 & 0 & 0 & 0 & 0 \\ 0 & 0 & 0 & 0 & 0 \\ 0 & 0 & 0 & 0 & 0 \end{matrix}\right] \tag{AII.2}$$

$\hat{B}_a(\theta)$ is derived analogously.

Artificial dissipation according to Eq. (26) is added to all gas phase equations, resulting in the following formulation for $\widehat{A}_d(\theta)$:

$$\widehat{A}_d(\theta) = \begin{bmatrix} 0 & 0 & 0 & 0 & 0 & 0 & 0 & 0 & 0 & 0 \\ 0 & (\delta_{\mathrm{ad}}/\beta_x)\cdot vi(\theta,\,\mathrm{d}x)\cdot \mathrm{d}x & 0 & 0 & 0 & 0 & 0 & 0 & 0 & 0 \\ 0 & 0 & 0 & 0 & 0 & 0 & 0 & 0 & 0 & 0 \\ 0 & 0 & 0 & 0 & 0 & 0 & 0 & 0 & 0 & 0 \\ 0 & (\delta_{\mathrm{ad}}/\beta_x)\cdot vi(\theta,\,\mathrm{d}x)\cdot \mathrm{d}x\cdot u_x & 0 & 0 & 0 & 0 & 0 & 0 & 0 & 0 \\ 0 & (\delta_{\mathrm{ad}}/\beta_x)\cdot vi(\theta,\,\mathrm{d}x)\cdot \mathrm{d}x\cdot u_y & 0 & 0 & 0 & 0 & 0 & 0 & 0 & 0 \\ 0 & (\delta_{\mathrm{ad}}/\beta_x)\cdot vi(\theta,\,\mathrm{d}x)\cdot \mathrm{d}x\cdot H_{\mathrm{g}} & 0 & 0 & 0 & 0 & 0 & 0 & 0 & 0 \\ 0 & 0 & 0 & 0 & 0 & 0 & 0 & 0 & 0 & 0 \\ 0 & (\delta_{\mathrm{ad}}/\beta_x)\cdot vi(\theta,\,\mathrm{d}x)\cdot \mathrm{d}x\cdot k & 0 & 0 & 0 & 0 & 0 & 0 & 0 & 0 \\ 0 & (\delta_{\mathrm{ad}}/\beta_x)\cdot vi(\theta,\,\mathrm{d}x)\cdot \mathrm{d}x\cdot \varepsilon & 0 & 0 & 0 & 0 & 0 & 0 & 0 & 0 \end{bmatrix} \tag{AII.3}$$

$\hat{B}_d(\theta)$ is derived analogously.

Using *vi*() given by Eq. (52), the viscous fluxes result in:

$$\widehat{A}_v(\theta) = \left[\begin{array}{ccccc}
0 & 0 & 0 & 0 & 0 \\
0 & 0 & 0 & 0 & 0 \\
0 & 0 & \left[\varepsilon_s \cdot \left(\xi_s - 2\mu_s 3^{-1}\right) + 2\varepsilon_s \mu_s\right] \cdot vi(\theta, dx) & 0 & 0 \\
0 & 0 & 0 & \varepsilon_s \mu_s \cdot vi(\theta, dx) & 0 \\
0 & 0 & 0 & 0 & \left[\varepsilon_g \cdot \left(\xi_g - 2\mu_g^{tot} 3^{-1}\right) + 2\varepsilon_g \mu_g^{tot}\right] \cdot vi(\theta, dx) \\
0 & 0 & 0 & 0 & 0 \\
0 & 0 & 0 & 0 & \left[\varepsilon_g \cdot \left(\xi_g - 2\mu_g^{tot} 3^{-1}\right) + 2\varepsilon_g \mu_g^{tot}\right] \cdot u_x \cdot vi(\theta, dx) \\
0 & 0 & 0 & 0 & 0 \\
0 & 0 & 0 & 0 & 0 \\
0 & 0 & 0 & 0 & 0
\end{array}\right. \tag{AII.4}$$

$$\left.\begin{array}{ccccc}
0 & 0 & 0 & 0 & 0 \\
0 & 0 & 0 & 0 & 0 \\
0 & 0 & 0 & 0 & 0 \\
0 & 0 & 0 & 0 & 0 \\
0 & 0 & 0 & 0 & 0 \\
\varepsilon_g \mu_g^{tot} \cdot vi(\theta, dx) & 0 & 0 & 0 & 0 \\
\varepsilon_g \mu_g^{tot} \cdot u_y \cdot vi(\theta, dx) & \varepsilon_g \lambda_g^{tot} \cdot vi(\theta, dx) & 0 & 0 & 0 \\
0 & 0 & \varepsilon_s \kappa \cdot vi(\theta, dx) & 0 & 0 \\
0 & 0 & 0 & \varepsilon_g \mu_g^{tot} \sigma_k^{-1} \cdot vi(\theta, dx) & 0 \\
0 & 0 & 0 & 0 & \varepsilon_g \mu_g^{tot} \sigma_\varepsilon^{-1} \cdot vi(\theta, dx)
\end{array}\right]$$

$\hat{B}_v(\theta)$ is derived analogously.

The part of the viscous fluxes related to non-neighbouring nodes results in the following contribution:

$$\widehat{D}_v(\theta, \theta b) = \left[\begin{array}{cccc}
0 & 0 & 0 & 0 \\
0 & 0 & 0 & 0 \\
0 & 0 & 0 & \left[\varepsilon_\mathrm{s} \cdot \left(\xi_\mathrm{s} - 2\mu_\mathrm{s} 3^{-1}\right) + \varepsilon_\mathrm{s} \mu_\mathrm{s}\right] \cdot vi2(\theta, \theta b, \mathrm{d}x, \mathrm{d}y) \\
0 & 0 & \left[\varepsilon_\mathrm{s} \cdot \left(\xi_\mathrm{s} - 2\mu_\mathrm{s} 3^{-1}\right) + \varepsilon_\mathrm{s} \mu_\mathrm{s}\right] \cdot vi2(\theta, \theta b, \mathrm{d}x, \mathrm{d}y) & 0 \\
0 & 0 & 0 & 0 \\
0 & 0 & 0 & 0 \\
0 & 0 & 0 & 0 \\
0 & 0 & 0 & 0 \\
0 & 0 & 0 & 0 \\
0 & 0 & 0 & 0
\end{array}\right.$$

$$\left.\begin{array}{ccc}
0 & 0 & 0\,0\,0\,0 \\
0 & 0 & 0\,0\,0\,0 \\
0 & 0 & 0\,0\,0\,0 \\
0 & 0 & 0\,0\,0\,0 \\
0 & \left[\varepsilon_\mathrm{g} \cdot \left(\xi_\mathrm{g} - 2\mu_\mathrm{g}^\mathrm{tot} 3^{-1}\right) + \varepsilon_\mathrm{g} \mu_\mathrm{g}^\mathrm{tot}\right] \cdot vi2(\theta, \theta b, \mathrm{d}x, \mathrm{d}y) & 0\,0\,0\,0 \\
\left[\varepsilon_\mathrm{g} \cdot \left(\xi_\mathrm{g} - 2\mu_\mathrm{g}^\mathrm{tot} 3^{-1}\right) + \varepsilon_\mathrm{g} \mu_\mathrm{g}^\mathrm{tot}\right] \cdot vi2(\theta, \theta b, \mathrm{d}x, \mathrm{d}y) & 0 & 0\,0\,0\,0 \\
\left[\varepsilon_\mathrm{g} \cdot \left(\xi_\mathrm{g} - 2\mu_\mathrm{g}^\mathrm{tot} 3^{-1}\right) + \varepsilon_\mathrm{g} \mu_\mathrm{g}^\mathrm{tot}\right] \cdot u_y \cdot vi2(\theta, \theta b, \mathrm{d}x, \mathrm{d}y) & \left[\varepsilon_\mathrm{g} \cdot \left(\xi_\mathrm{g} - 2\mu_\mathrm{g}^\mathrm{tot} 3^{-1}\right) + \varepsilon_\mathrm{g} \mu_\mathrm{g}^\mathrm{tot}\right] \cdot u_x \cdot vi2(\theta, \theta b, \mathrm{d}x, \mathrm{d}y) & 0\,0\,0\,0 \\
0 & 0 & 0\,0\,0\,0 \\
0 & 0 & 0\,0\,0\,0 \\
0 & 0 & 0\,0\,0\,0
\end{array}\right], \tag{AII.5}$$

where *vi*2() is given by Eq. (53).

The gravity source terms result in:

$$G_R = \begin{pmatrix} 0 & 0 & 0 & 0 & 0 & 0 & 0 & 0 & 0 & 0 \\ 0 & 0 & 0 & 0 & 0 & 0 & 0 & 0 & 0 & 0 \\ \rho_{sp} g_x & 0 & 0 & 0 & 0 & 0 & 0 & 0 & 0 & 0 \\ \rho_{sp} g_y & 0 & 0 & 0 & 0 & 0 & 0 & 0 & 0 & 0 \\ -\rho_{sp} g_x & 0 & 0 & 0 & 0 & 0 & 0 & 0 & 0 & 0 \\ -\rho_{sp} g_y & 0 & 0 & 0 & 0 & 0 & 0 & 0 & 0 & 0 \\ -\rho_{sp}\left(g_x u_x + g_y u_y\right) & 0 & 0 & 0 & -\varepsilon_s \rho_{sp} g_x & -\varepsilon_s \rho_{sp} g_y & 0 & 0 & 0 & 0 \\ 0 & 0 & 0 & 0 & 0 & 0 & 0 & 0 & 0 & 0 \\ 0 & 0 & 0 & 0 & 0 & 0 & 0 & 0 & 0 & 0 \\ 0 & 0 & 0 & 0 & 0 & 0 & 0 & 0 & 0 & 0 \end{pmatrix}. \tag{AII.6}$$

The drag source terms, on the other hand, result in:

$$D_R = \begin{pmatrix} 0 & 0 & 0 & 0 & 0 & 0 & 0 & 0 & 0 & 0 \\ 0 & 0 & 0 & 0 & 0 & 0 & 0 & 0 & 0 & 0 \\ 0 & 0 & -\beta & 0 & \beta & 0 & 0 & 0 & 0 & 0 \\ 0 & 0 & 0 & -\beta & 0 & \beta & 0 & 0 & 0 & 0 \\ 0 & 0 & \beta & 0 & -\beta & 0 & 0 & 0 & 0 & 0 \\ 0 & 0 & 0 & \beta & 0 & -\beta & 0 & 0 & 0 & 0 \\ 0 & 0 & \beta v_x & \beta v_y & -\beta u_x & -\beta u_y & 0 & 0 & 0 & 0 \\ 0 & 0 & 0 & 0 & 0 & 0 & 0 & 0 & 0 & 0 \\ 0 & 0 & 0 & 0 & 0 & 0 & 0 & 0 & 0 & 0 \\ 0 & 0 & 0 & 0 & 0 & 0 & 0 & 0 & 0 & 0 \end{pmatrix}. \tag{AII.7}$$

References

[1] K. Agrawal, P.N. Loezos, M. Syamlal, S. Sundaresan, The role of meso-scale structures in rapid gas–solid flows, J. Fluid Mech. 445 (2001) 151–185.

[2] T. Anderson, R. Jackson, A fluid mechanical description of fluidized beds, Ind. Eng. Chem. Fundam. 6 (1967) 527.

[3] J. De Wilde, Adsorption of SO_2 and NO_x in a Riser: kinetics and 3D gas–solid hydrodynamics. Ph.D. dissertation, Universiteit Gent, Belgium, 2001.

[4] J. De Wilde, G.J. Heynderickx, J. Vierendeels, E. Dick, G.B. Marin, An extension of the preconditioned advection upstream splitting method for 3D two-phase flow calculations in circulating fluidized beds, Comp. Chem. Eng. 26 (12) (2002) 1677–1702.

[5] J. De Wilde, G.B. Marin, G.J. Heynderickx, The effects of abrupt T-outlets in a riser: 3D simulation using the kinetic theory of granular flow, Chem. Eng. Sci. 58 (3-6) (2003) 877–885.

[6] J. De Wilde, G.J. Heynderickx, G.B. Marin, A gradient instead of a source term approach for gas–solid Interactions in Eulerian–Eulerian gas–solid flow models. In: Proceedings of the 5th International Conference on Multiphase Flow (ICMF-2004), Yokohama, Japan, May 30–June 3, 2004.

[7] E. Dick, J. Steelant, Coupled solution of the steady compressible Navier–Stokes equations and the *k*–epsilon turbulence equations with a multigrid method, Appl. Numer. Math. 23 (1) (1997) 49–61.

[8] J. Ding, D. Gidaspow, A bubbling fluidization model using kinetic-theory of granular flow, AIChE J. 36 (4) (1990) 523–538.

[9] S. Evje, T. Flatten, Hybrid flux-splitting schemes for a common two-fluid model, J. Comput. Phys. 192 (1) (2003) 175–210.

[10] S. Evje, K.K. Fjelde, On a rough AUSM scheme for a one-dimensional two-phase model, Comput. Fluids 32 (10) (2003) 1497–1530.

[11] R.O. Fox, Computational methods for turbulent reacting flows in the chemical process industry, Rev. I. Fr. Petrol. 51 (2) (1996) 215–243.

[12] D. Gidaspow, Multiphase Flow and Fluidization: Continuum and Kinetic Theory Descriptions, Academic Press, London, 1994.

[13] W. Gregor, H. Rumpf, Velocity of sound in two-phase media, Int. J. Multiphase Flow 1 (6) (1975) 753–769.

[14] F.H. Harlow, A.A. Amsden, Numerical-calculation of multiphase fluid-flow, J. Comput. Phys. 17 (1) (1975) 19–52.

[15] J. Hinze, Turbulence: an Introduction to Its Mechanism and Theory, McGraw-Hill, New York, 1959.

[16] J.A.M. Kuipers, K.J. Vanduin, F.P.H. Vanbeckum, W.P.M. Vanswaaij, A numerical-model of gas-fluidized beds, Chem. Eng. Sci. 47 (8) (1992) 1913–1924.

[17] M.-S. Liou, C.J. Steffen, A new flux splitting scheme, J. Comput. Phys. 107 (1) (1993) 23–39.

[18] M.-S. Liou, J.R. Edwards, AUSM schemes and extensions for low-Mach and multiphase flows, in: Proceedings of the 30th Computational Fluid Dynamics, Von Karman Institute for Fluid Dynamics Lecture Series 1999–2003, 1999.

[19] D.M. Mao, J.R. Edwards, A.V. Kuznetsov, R.K. Srivastava, Development of low-diffusion flux-splitting methods for dense gas–solid flows, J. Comput. Phys. 185 (1) (2003) 100–119.

[20] J.J. Nieuwland, M.V. Annaland, J.A.M. Kuipers, W.P.M. vanSwaaij, Hydrodynamic modeling of gas/particle flows in riser reactors, AIChE J. 42 (6) (1996) 1569–1582.

[21] H. Paillère, C. Corre, J.R.G. Cascales, On the extension of the AUSM plus scheme to compressible two-fluid models, Comput. Fluids 32 (6) (2003) 891–916.

[22] S.V. Patankar, D.B. Spalding, Calculation procedure for heat, mass and momentum-transfer in 3-dimensional parabolic flows, Int. J. Heat Mass Transfer 15 (10) (1972) 1787.

[23] W.C. Rivard, M.D. Torrey, K-Fix: A Computer Program for Transient, Two-dimensional, Two-fluid Flow, Los Alamos, La-Nureg-6623, 1977.

[24] W.C. Rivard, M.D. Torrey, Threed: An Extension of the K-Fix Code for Three Dimensions, Los Alamos, La-Nureg-6623, 1979.

[25] A. Samuelsberg, B.H. Hjertager, Computational modeling of gas/particle flow in a riser, AIChE J. 42 (6) (1996) 1536–1546.

[26] H. Schlichting, Boundary-Layer Theory, Seventh ed., McGraw-Hill, New York, 1979.

[27] J.L. Sinclair, R. Jackson, Gas-particle flow in a vertical pipe with particle–particle interactions, AIChE J. 35 (9) (1989) 1473–1486.

[28] H.B. Stewart, B. Wendroff, 2-Phase flow – models and methods, J. Comput. Phys. 56 (3) (1984) 363–409.

[29] E. Turkel, Preconditioned methods for solving the incompressible and low-speed compressible equations, J. Comput. Phys. 72 (2) (1987) 277–298.

[30] J. van der Schaaf, J.C. Schouten, C.M. van den Bleek, Origin, propagation and attenuation of pressure waves in gas–solid fluidized beds, Powder Technol. 95 (3) (1998) 220–233.

[31] G. Van engelandt, J. De Wilde, G.J. Heynderickx, G.B. Marin, Experimental study on the inlet phenomena of a 35° inclined non-aerated and aerated Y-inlet in a dilute cold-flow riser, Int. J. Multiphase Flow (submitted).

[32] J. Vierendeels, K. Riemslagh, E. Dick, A multigrid semi-implicit line-method for viscous incompressible and low-Mach-number flows on high aspect ratio grids, J. Comput. Phys. 154 (2) (1999) 310–341.

[33] J. Vierendeels, B. Merci, E. Dick, Blended AUSM plus method for all speeds and all grid aspect ratios, AIAA J. 39 (12) (2001) 2278–2282.

[34] J.M. Weiss, W.A. Smith, Preconditioning applied to variable and constant density flows, AIAA J. 33 (11) (1995) 2050–2057.

[35] D.Z. Zhang, W.B. VanderHeyden, The effects of mesoscale structures on the macroscopic momentum equations for two-phase flows, Int. J. Multiphase Flow 28 (5) (2002) 805–822.